EFFECT OF WIDTH-TO-DEPTH RATIO ON THE MEAN FLOW VELOCITIES FOR A KINOSHITA MEANDER BEND.

BY

ROBERTO FERNÁNDEZ ARRIETA

THESIS

Submitted in partial fulfillment of the requirements
for the degree of Master of Science in Civil Engineering
in the Graduate College of the
University of Illinois at Urbana-Champaign, 2012

Urbana, Illinois

Adviser:

Professor Marcelo H. García

ABSTRACT

The present work analyses the effect of different width-to-depth ratios on the mean surface velocities of a Kinoshita meander bend. The characteristics of flow in such a bend have been studied by Ancalle (2007) and Abad and Garcia (2009a) for width-to-depth ratios equal to 2.4 and 4.0. The present study extends that work and includes a higher width-to-depth ratio (equal to 12.0) in addition to those already studied.

The main difference between previous studies and the current one is the technique used to measure. Particle Tracking Velocimetry (PTV), a non-intrusive technique, was adopted here to take the measurements. The technique allows measuring in the Kinoshita flume for higher width-to-depth ratios than it is feasible with the use of other techniques such as Acoustic Doppler Velocimeters (ADVs).

The results obtained from the measurements are also used to validate a 2D depth-averaged rigid-lid model called STREMR (Bernard (1993)). The model has an empirical correction for secondary flow which is evaluated in light of the values obtained from the measurements. Results obtained with the model are in good agreement with the measurements taken, showing that STREMR is an adequate tool to model flows in bends even if they are not shallow.

Measured and modeled values indicate that different width-to-depth ratios have similar patterns but the secondary flow intensity is different in all of them, thus modifying the time required for the core of high velocities to migrate from the inner part of the bend to the outer part. Velocity turnover in regions of low curvature happens at slightly different locations for the different width-to-depth ratios suggesting that the secondary flow intensity plays

a role in it.

Al Todo y a mi familia por tantas alegrías.

TABLE OF CONTENTS

CHAPTER 1

INTRODUCTION

Flow in meandering channels has been studied since the late 1800s (e.g. Thomson (1876)) and continues to be an intriguing research area. As new understanding is obtained of the processes underlaying it and as technology evolves both to measure and to perform numerical simulations, the hydrodynamics and their linkage to the morphodynamics of meander bends continue to be unraveled. This study combines experiments and modeling of flow in a high-amplitude Kinoshita meander bend for different width-to-depth ratios on a non-movable flat bed. Experimental measurements used a non-intrusive technique, namely Particle Tracking Velocimetry (PTV) and the modeling was conducted with STREMR (Bernard (1993), Abad et al. (2008)), a 2D depth-averaged model which was validated against the experimental data.

1.1 Background

Flow in meandering channels has been studied for decades in order to understand the characteristics of flow in bends, secondary flow cells, superelevation, flow resistance and bed morphodynamics. Thomson (1876) presented a description of the reason why rivers tend to migrate in alluvial plains, discussing the cause of transverse slope in the water surface in a bend and its effects in the velocity patterns as well as on the erosion of the outer bank and deposition on the inner bank.

In the 1930s researchers were interested in the characteristics of flow around bends (Nippert (1930); Blue and Lancefield (1934); Boss (1934); Yarnell and Woodward (1936); Raju (1937)), the sediment load distribution on them (Eakin (1935)) and the effect of curvature on fully-developed turbulent flow (Wattendorf (1935)). During the 1940s experimental and theoretical studies

were presented which dealt with the effects of channel shape on losses in a canal bend (Yen and Howe (1942)), flow around bends in stable channels (Mockmore (1944)) and meandering of alluvial rivers (Friedkin (1945)).

The following six decades saw increasing interest of both engineers and geologists in the characteristics of flow in bends. Both communities attempted describing the hydrodynamics and morphodynamics by developing and implementing models (Langbein and Leopold (1966); Ikeda et al. (1981); Parker et al. (1982); Parker (1983); Johannesson and Parker (1989); Odgaard (1986); Odgaard (1989); Garcia et al. (1994); Howard (1996); Seminara and Zolezzi (2001); Darby (2002); Lancaster and Bras (2002); Abad and García (2004)), by conducting laboratory experiments (Shukry (1950); Fedorov (1954); Rozovskii (1961); Yen (1965); Schumm and Kahn (1971); Parker and Andrews (1985); Whiting and Dietrich (1993b); Whiting and Dietrich (1993a)) and by doing field measurements and observations (Leopold and Wolman (1960); Zeller (1967); Brice (1973); Bridge and Jarvis (1976); Allen (1982)).

During the last years attention has been put more specifically into their migration patterns and stability due to re-naturalization techniques which in some cases involve re-meandering streams. To this effect recent experimental studies have focused on the hydraulics of high-amplitude meandering bends Ancalle (2007)) the implications of bend orientation on mean and turbulent flow structure (Abad and Garcia (2009a)) and on bed morphodynamics (Abad and Garcia (2009b)), flow fields in meander bends of low width-to-depth ratio (Nanson (2009)) and the variation of flow patterns with sinuosity (da Silva et al. (2007)).

Modeling of meander migration has continued to evolve accounting for physical processes such as bank erosion (Motta et al. (2011)), width changes and riparian vegetation (Eke and Parker (2010)) and a new framework for modeling the migration of meandering rivers has recently been proposed (Parker et al. (2011)). In order to validate this new approaches more experimental and field data is necessary due to the fact that the structure of secondary flow cells varies with curvature, width-to-depth ratio, bed topography and flow intensity. The experiments mentioned above address some of these aspects but there is still room to study the effect of width-to-depth ratio on the flow

structure of high-amplitude meander bends.

A very quick and practical way of getting a flow velocity estimate on a given natural or man made channel is by putting some tracers on the water and measuring the time they take to move a certain distance. Such a simplistic approach forms the basis for flow velocity measurements using Particle Image Velocimetry (PIV) and Particle Tracking Velocimetry (PTV). The latter is used in this study to analyze the flow patterns in a Kinoshita meander bend for three different width-to -depth ratios on a non-movable flat bed condition. The underlying assumption for the technique is that the tracer particles closely follow the flow, i.e. they travel at the same velocity as the flow.

PTV was originally developed to analyze images which had low particle density and instead of working in an Eulerian framework, the algorithms were constructed in a Lagrangian framework. To analyze the data, different algorithms with varying degrees of sophistication have been proposed (Hassan et al. (1992); Lloyd et al. (1995); Baek and Lee (1996); Ishikawa et al. (2000); Ohmi and Li (2000); Kim and Lee (2002); Ruhnau et al. (2005); Mikheev and Zubstov (2008)). Recently, Brevis (2011) proposed a hybrid approach which combines the cross-correlation and relaxation algorithms for particle tracking velocimetry. This technique allows analyzing images with different flow and seeding conditions and has proven to have high performance in terms of the resulting vector fields.

Abad and Garcia (2009a) and Ancalle (2007) did experiments on the Kinoshita flume used in this study. Both of them used Acoustic Doppler Velocimeters (ADVs) to measure the flow properties. Nevertheless, the width of the flume and the geometry of this instrument impede measuring the flow properties for high width-to-depth ratios. Even if a side looking probe such as that in the Vectrino was used, the highest feasible width-to-depth ratio that could be measured is smaller than 10. Therefore, the non-intrusive PTV approach was followed to conduct the experiments.

1.2 Motivation

Experiments in a high-amplitude Kinoshita meander bend performed at the University of Illinois have explored the implications of bend orientation in mean and turbulent flow structure Abad and Garcia (2009a) as well as on bed morphodynamics Abad and Garcia (2009b). The present's study motivation is to extend that work taking into account higher width-to-depth ratios on a non-movable flat bed condition.

Previous studies as the one by Ancalle (2007) and those mentioned above used Acoustic Doppler Velocimeters (ADVs) to measure flow velocities. However, velocities for high width-to-depth ratios (larger than 10) are not easy to measure in the Kinoshita flume due to its limited width (0.60 m) and the geometric properties of ADVs. Therefore, in order to get some insight on the mean flow structure in high-amplitude meander bends for higher width-to-depth ratios a non-intrusive approach has been followed using Particle Tracking Velocimetry (PTV) on the water surface.

1.3 Objectives

1.3.1 Main Objective

The main objective of this work is to determine the differences in mean surface flow structure for different width-to-depth ratios in a high-amplitude, upstream skewed Kinoshita meander bend with a non-movable flat bed.

1.3.2 Specific Objectives

1. Learn how to measure and process data using the Particle Tracking Velocimetry (PTV) technique.

2. Determine mean surface velocity and mean surface vorticity for three different width-to-depth ratio conditions in one full bend of the Kinoshita flume for an upstream skewed configuration.

3. Learn how to set up and run the 2D depth-averaged rigid lid model STREMR (Bernard (1993), Abad et al. (2008)).

4. Validate the numerical model against the measurements.

5. Assess the impact of the secondary flow correction routines of the model on the flow in light of the comparison with measured values.

1.4 Thesis Outline

The present work is organized in six chapters. The current chapter, which is introductory, dealt with the objectives of the work as well as the background and motivation for the experiments. The experimental setup is described in Chapter 2 where details about the flume and instruments used are given. Chapter 3 deals with theoretical and practical aspects on the Particle Tracking Velocimetry Technique employed to measure. The characteristics of the 2D depth-averaged model and its implementation are described in Chapter 4. Chapter 5 presents the results and comparison among the three different width-to-depth ratios in terms of surface mean flow characteristics. It also includes the 2D depth-averaged rigid lid model validation. Chapter 6 presents the conclusions of the work and some recommendations for future research on the topic.

CHAPTER 2

EXPERIMENTAL METHOD

The flume in which the experiments were carried out is described in this section along with the experimental setup. The characteristics of the equipment used as well as the three experimental conditions are summarized.

2.1 The Flume

The set of experiments presented in this study were conducted in the Kinoshita flume at the Ven Te Chow Hydrosystems Laboratory (see Figure 2.1). The plan form shape of this flume was designed after the Kinoshita curve (Parker (1983)). This generates a sinusoidal shape capable of resembling the course of meandering channels by taking into account the flatness and skewness of meander bends. The equation for the Kinoshita curve is Eq. (2.1):

$$\theta = \theta_0 sin\left(\frac{2\pi s}{\lambda}\right) + \theta_0^3\left[J_s cos\left(3\frac{2\pi s}{\lambda}\right) - J_f sin\left(3\frac{2\pi s}{\lambda}\right)\right] \qquad (2.1)$$

where

J_s – Skewness coefficient.

J_f – Flatness coefficient.

θ_0 – Maximum angular amplitude at the inflection point.

λ – Channel length over the meandering period.

The values of the Kinoshita flume are

$J_s = \pm\frac{1}{32}$; positive for upstream skewness and negative for downstream skewness.

$J_f = \frac{1}{192}$.

$\theta_0 = 110^o$.

The planview schematic of the flume is shown in Figure 2.1. It is 32 m long with three high-amplitude meander bends (each 10 m long) with a width of 0.60 m, a maximum depth of 0.40 m and longitudinal and transversal slopes of zero (horizontal bed). The flume is made of Plexiglas and therefore is smooth. Reservoirs located at each end of the flume are connected by a piping network that allows recirculating water by a centrifugal pump. Flow can be reversed to run a different skewness condition (upstream or downstream skewed). It can also be used with sediment (e.g. Abad and Garcia (2009b)) by using another centrifugal pump to recirculate a water-sediment mix. More details on the flume can be found in Ancalle (2007), Abad and Garcia (2009a).

2.2 Instrumentation

The basic experimental set up is shown in Figure 2.2. It consists of a rigid metallic frame to hold the camera, a set of LED panels and a halogen to enhance lighting in the measured section. The camera used is a TSI Y5 with a 28 mm Nikon lens located approximately 1.35 m above the flume's bed. A software called *Motion Studio* was used to set up each measurement and download it from the camera. Discharge into the channel was measured using a magnetic flow meter installed at the suction pipe of the pump and it was controlled with a valve.

2.3 The Experiments

Particle tracking on the full middle bend of the Kinoshita flume (stations 10 to 20) was made for three different width-to-depth ratios with an upstream skewed configuration. The main characteristics of each of those experiments are summarized in Table 2.1. Depth was measured with no flow conditions at the upstream tank. Experiments one and two used the same flow discharge while experiments two and three have approximately the same reach-averaged velocity. The camera used had enough memory to store 837 images. A frequency of 50 Hz was used which allows measuring continually for 16,74

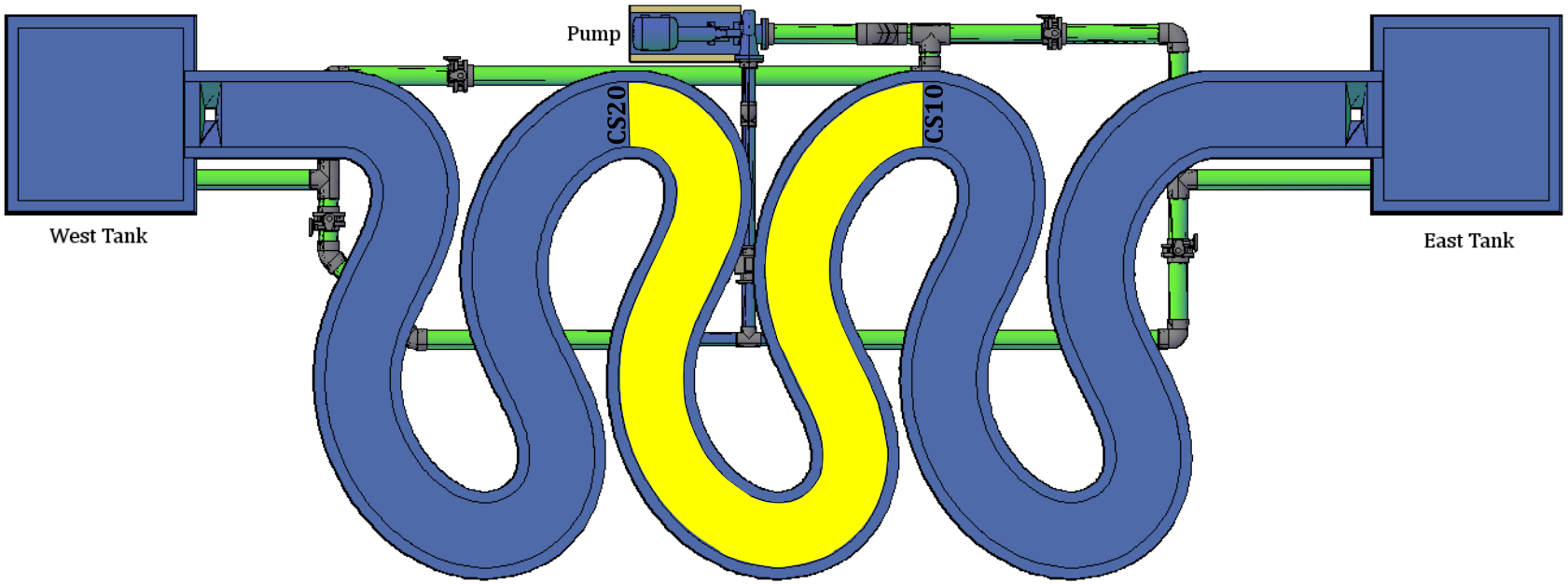

Figure 2.1: Plan view schematic of the Kinoshita Flume. The highlighted zone (CS10-CS20) corresponds to the region where measurements were taken.

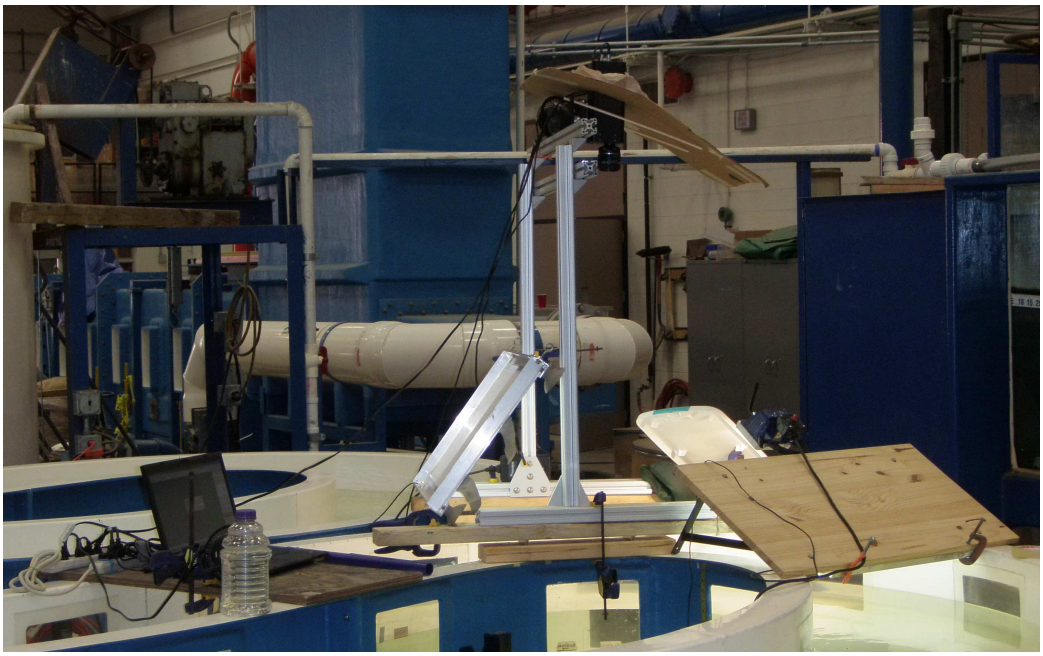

Figure 2.2: Basic experimental set up.

Table 2.1: Experimental Conditions.

Property		**Experiment No.**		
		1	**2**	**3**
Depth	$[m]$	0.25	0.15	0.05
Width-to-Depth Ratio	$[-]$	2.4	4.0	12.0
Flow	$[L/s]$	25	25	8
Reach-Averaged Velocity	$[m/s]$	0.17	0.28	0.27
Froude Number	$[-]$	0.11	0.23	0.38
Reynolds Number	$[-]$	22,282	27,233	11,204

s. Ten independent sets of measurements were taken at each location to be able to obtain the mean surface flow characteristics.

CHAPTER 3

PARTICLE TRACKING VELOCIMETRY

Particle Tracking Velocimetry (PTV) is used in studies where the density of tracer particles is low. This lower density differentiates PTV from Particle Image Velocimetry (PIV) mainly in the possibility of extracting velocity vectors on a particle by particle basis (Langrangean approach). These vectors which will have an unstructured distribution across the image plane can later be post processed to obtain a structured distribution of the flow field. The basics of the technique are summarized in the following sections.

3.1 The Technique

Image processing routines are mainly based upon matrix algebra. Each image is treated as a matrix containing light intensity values on each element. The elements of the image (pixels) correspond to an i^{th}, j^{th} element of the matrix upon which operations can be performed. The different stages of the PTV technique operate on the images (matrices) in different ways until a result is obtained (e.g. a mean velocity field). Some stages are optional and some require some trial and error to adjust to the data being dealt with but in general is a simple and useful technique to obtain velocity vectors of a given flow.

3.2 Image Pre-Processing Routines

Three steps are required before running the specific particle tracking routines of detection and matching, namely: image inversion, background elimination and image masking.

3.2.1 Image Inversion

Images are acquired in a gray scale divided into 256 elements in which a value of 0 represents black and a value of 255 represents white as shown in Figure 3.1. Particle detection algorithms used here are based on the fact that particles are lighter in color than the background but this is not the case for the current experiments. Dark colored particles were used over a light colored background. Therefore the images need to be inverted which means that a dark colored particle in the original image will have a light color in the inverted image as shown in Figure 3.2. The inversion process simply subtracts 255 to each pixel in the image and then takes the absolute value of the result as the new value for that pixel. The operation can be described with Eq. (3.1).

$$P^{-1} = |P - 255| \tag{3.1a}$$

$$p_{i,j}^{-1} = |p_{i,j} - 255| \tag{3.1b}$$

where

P **-** Image as a matrix with values of light intensity in gray-scale.

p **-** Picture element (pixel) or the i^{th}, j^{th} element of matrix P.

P^{-1}, $p_{i,j}^{-1}$ **-** Inverted image (matrix) or pixel.

Figure 3.1: Gray scale in which images are acquired.

3.2.2 Background Elimination

The first step towards eliminating the background of all pictures in the series is to compute a mean image. This image will only show the things that remained fixed during the series, i.e. only the flume and the water surface will show up without the particles. An example mean image is presented in Figure 3.3. The process represented in that figure is attained iteratively

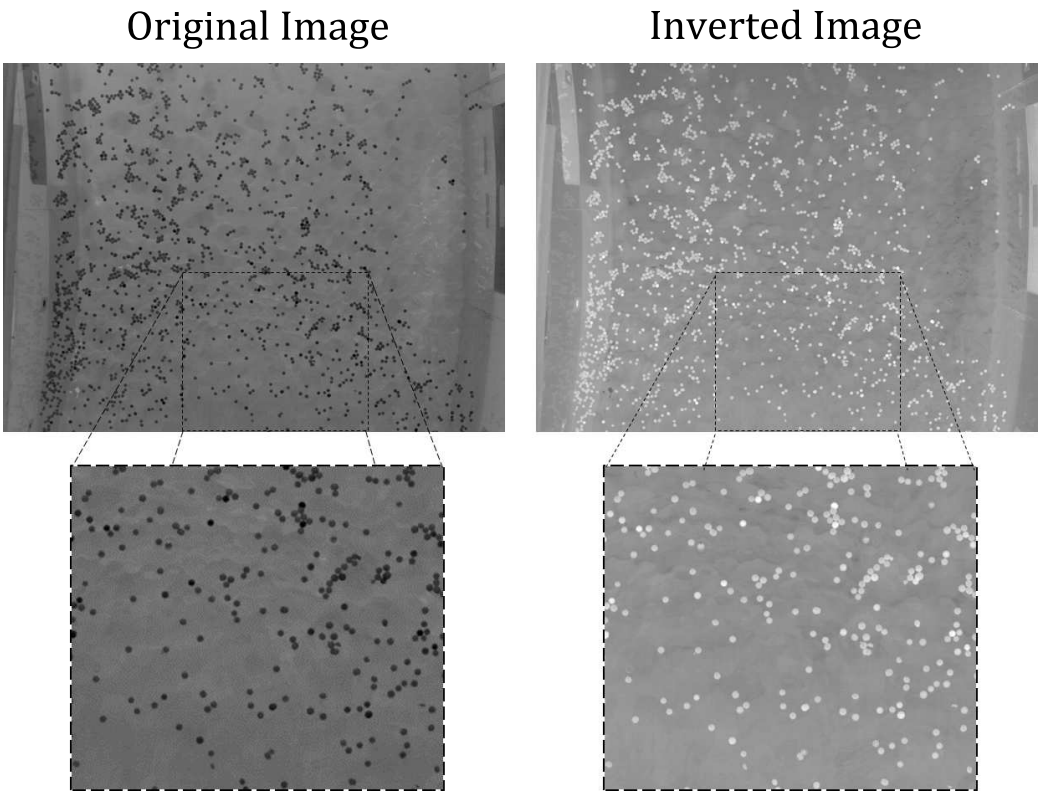

Figure 3.2: Original and associated inverted image are shown. Dark colors in the original frame become light colors in the inverted frame.

in the algorithms to avoid saturating the computer's memory by applying Eq. (3.2), to the image series;

$$M_j = \frac{M_{j-1} \cdot (j-1) + P_j}{j}; \qquad j = 1, 2, ..., n-1, n \tag{3.2}$$

where

M_j - Mean image of the series up to index j (current iteration).

M_{j-1} - Mean image of the series up to index $j-1$ (previous iteration).

P_j - j^{th} image in the series.

Note that when the value of j is equal to the total number of images in the series, the value of M will correspond to the mean image of that series. Once the mean image has been computed it is used to subtract from all images in the series the areas that did not move (i.e. everything that was not a particle). This is the actual process of background elimination and is applied to every image in the series. It is graphically represented in Figure 3.4 and mathematically in Eq. (3.3).

$$P_{NB_j} = P_j - M_n \tag{3.3}$$

where

P_{NB_j} - j^{th} picture in the series with no background.

P_j - j^{th} picture in the series.

M_n - Series' mean image.

3.2.3 Image Masking

The last step which in some cases might be considered optional is called masking. The main idea of the process is to discard areas of the image and by doing so saving some time in the routines of particle detection and particle matching. Masking can be done for any of the following reasons:

(a) The analysis needs to focus only on a specific area of the image.

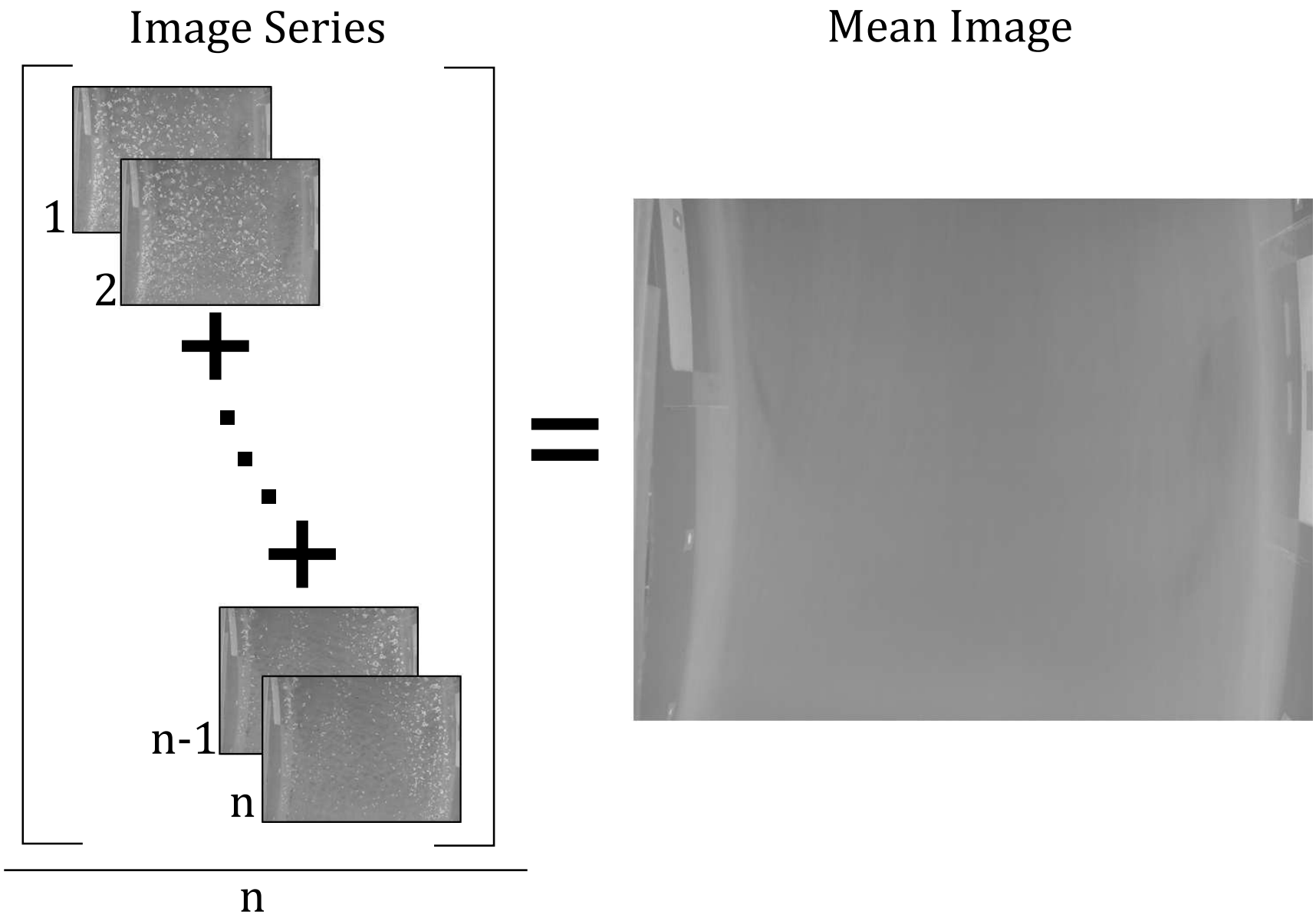

Figure 3.3: Schematic of the process by which the mean image is obtained.

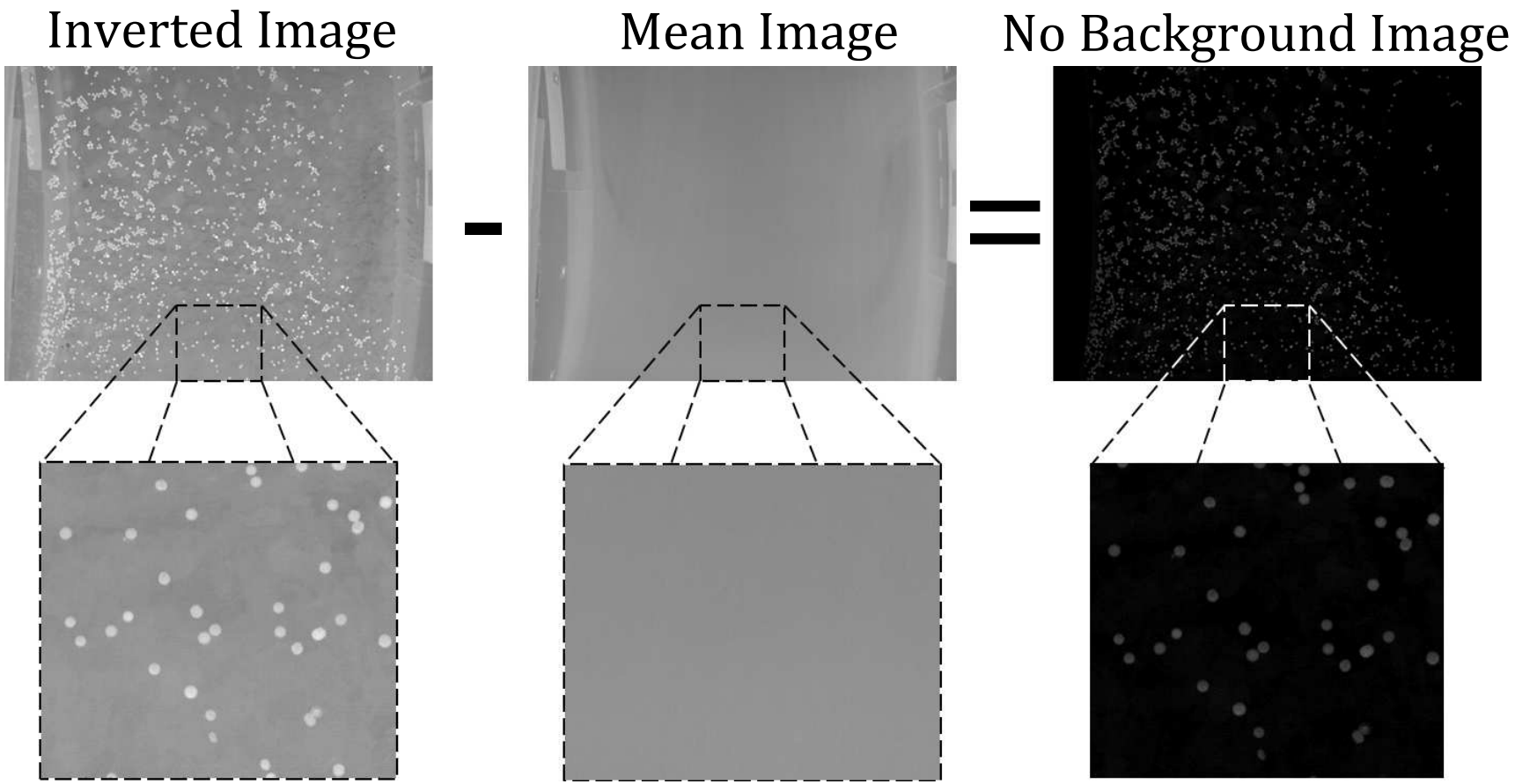

Figure 3.4: Schematic of image background removal showing the original inverted image and the resulting image after the mean has been subtracted.

(b) There are areas of the image in which there was no flow (e.g. obstacles, flume walls, etc.).

The latter option justifies the use of the masking algorithms in this work and it is used to discard the flume's walls from every image. The mask applied to all images is a binary matrix where the areas to be kept have a value of 1 and the areas to be discarded have a value of zero (see Eq. (3.4)).

$$mask = \begin{cases} i,j = 0 & \text{discard} \\ i,j = 1 & \text{keep} \end{cases} \tag{3.4}$$

The process of masking requires multiplying each image in the series by the mask. Figure 3.5 shows the process where a given image is multiplied by a binary image (white areas have a value equal to one and black areas have a value equal to zero). Only part of the image is kept for further processing and the rest is discarded.

3.3 Image Detection Routines

Each pixel in an image has a light intensity value associated. In the case of the original images, dark particles have low intensities and the flume has higher intensities. On the other hand, the images that were created during preprocessing stages will present high intensities associated with particles and low intensities associated with the background. Intensities are not constant throughout the image and not even within a particle itself. Nevertheless, the particle light intensity profile can be represented by a Gauss kernel and this is the basis of the Gaussian Particle Detection (GPD) routines.

3.3.1 Creating the Kernel

Kernel creation relies on one parameter in particular which is the representative radius of the particles in pixels. Kernel shape modifiers can be used if light intensities were very low or very high, or if optical distortion might have occurred in any axis (elongated particles instead of circular). The kernel is

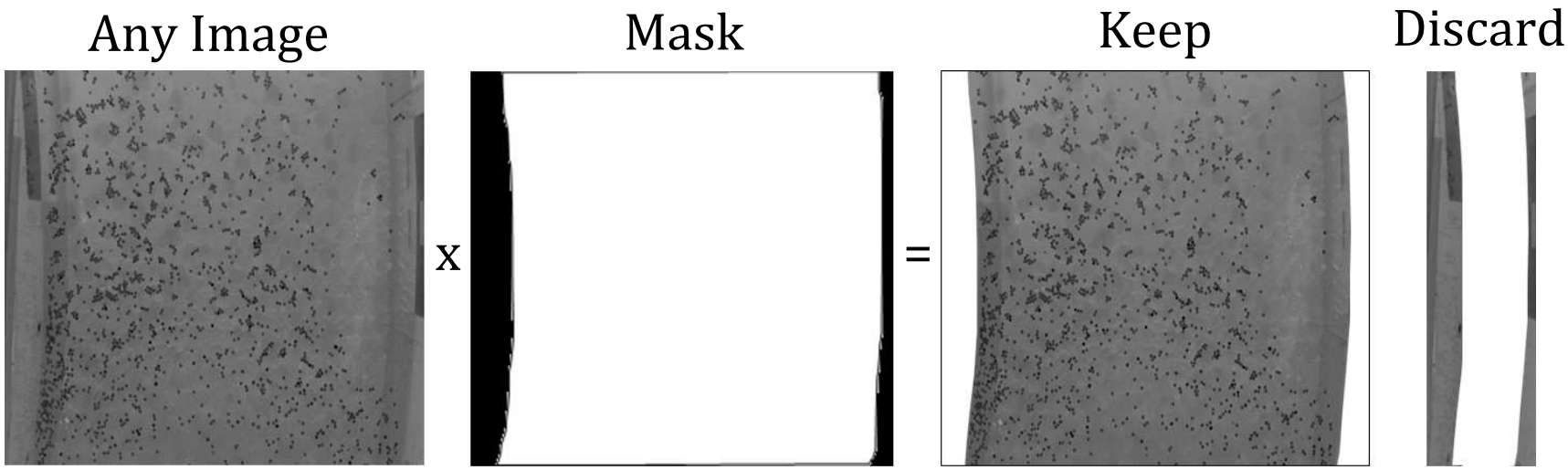

Figure 3.5: Schematic representing the image masking process.

created as shown in Eq. (3.5).

$$g_m = e^{-\left[\frac{(x-c)^2+(y-c)^2}{2\sigma}\right]} \tag{3.5}$$

Where:

σ **-** Representative radius of the particle in pixels.

c **-** is computed according to Eq. (3.6).

The value of c is used to obtain m (see Eq. (3.7)) which is required to generate the matrices x and y (see Eq. (3.9)) . The value of c is recomputed with Eq. (3.8) after m is determined. Note that the ceiling function yields the smallest following integer.

$$c = round\left(\frac{3}{4}\,\sigma\right) \tag{3.6}$$

$$m = 2c + 1 \tag{3.7}$$

$$c = ceil\left(\frac{m}{2}\right) \tag{3.8}$$

$$x(i,j) = i; \tag{3.9a}$$

$$y(i,j) = j; \tag{3.9b}$$

$$i = j = 1, 2, ..., m-1, m \tag{3.9c}$$

3.3.2 Threshold Level Definition

The first step towards finding the particles is actually finding the locations in the image in which there might be particles. This is done by defining a light intensity threshold value below which pixels will be considered part of the background and not used in further analysis. Pixels having higher intensity values will be kept for the next stage which is the particle centroid detection itself.

Figure 3.6 presents the original image and a set of images that show how the

threshold level acts preserving (discarding) pixels for the next stage. Note that a value between 25 and 35 would work well for the example shown; while preserving enough data it discards most of the cloudy areas observed at the center and bottom left region (especially for the case with a value of 5). Once the threshold level is defined, information about the position of each pixel that has a higher light intensity is saved and passed on to the next stage.

3.3.3 Particle Centroid Detection

Centroid detection uses correlation to determine if a pixel is the centroid of a particle by comparing the light intensity values around it (up to a representative particle radius of distance) with the kernel defined at a previous stage. If the pixel is located at the border of the particle the correlation will be very low but if it's located at or very close to the center, correlation will be high.

The process is iterative and involves analyzing each location passed from the previous stage and determining correlation between that pixel and the Gaussian kernel. For all pixels with values higher than the threshold level, correlation is computed and stored. When all possible particle locations have been correlated to the gauss kernel, a filtering process takes place to avoid detecting more than one centroid for a given particle or to be able to identify two particles that were travelling close together.

A correlation cut (threshold) must be defined a priori above which the locations will be accepted as particle centroids. A value of 1 would indicate that the light intensity distribution for any given particle must match exactly with the Gauss kernel defined above while lower values will allow for deviations from the Gauss kernel. Figure 3.7 shows the number of centroids found depending on the correlation cut value used.

3.4 Particle Matching Routines

Particle matching requires a pair of subsequent images from the series. The process consists in establishing candidate particles in the second frame that

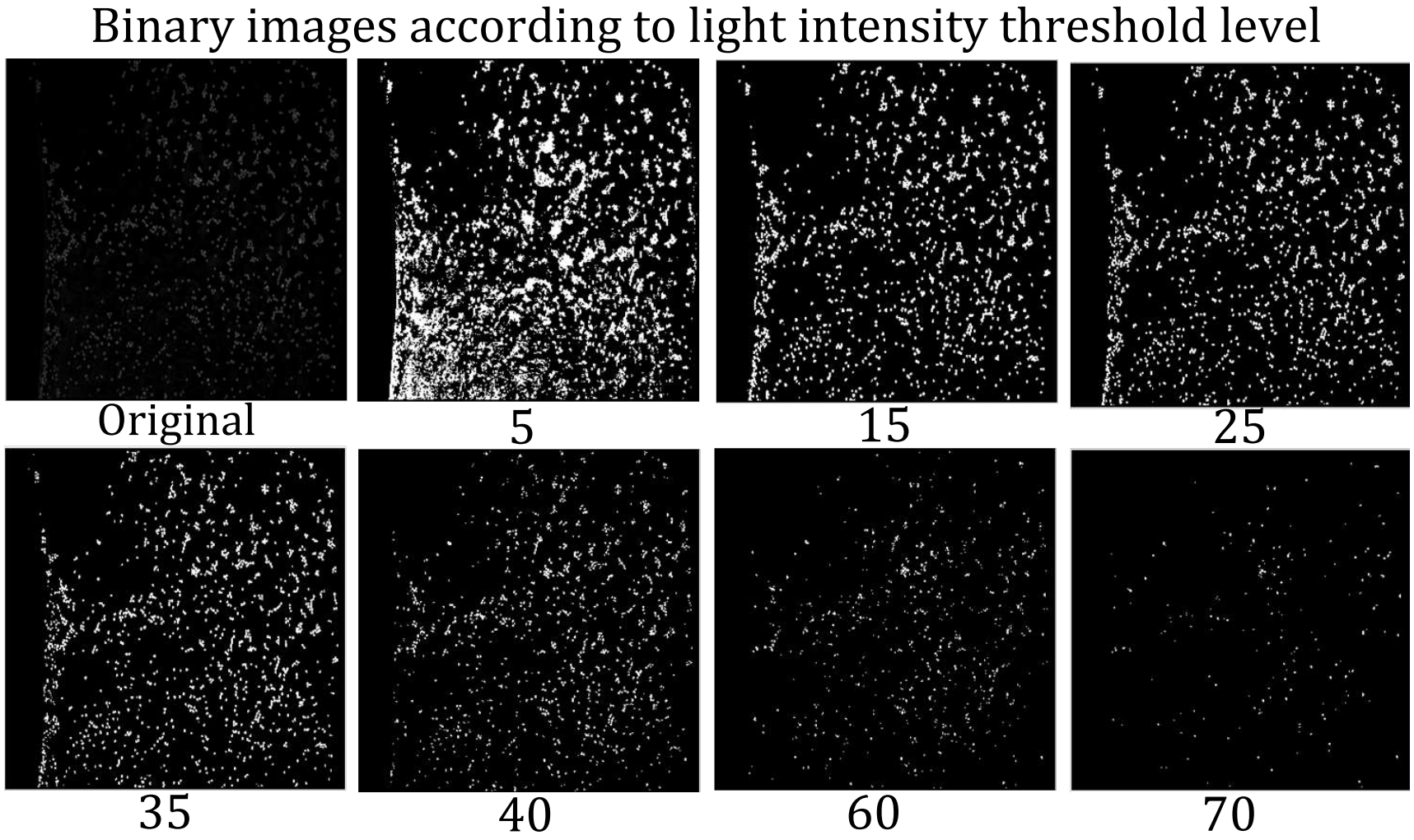

Figure 3.6: Binary images showing the effect of the light intensity threshold level in the number of particles detected by the algorithm.

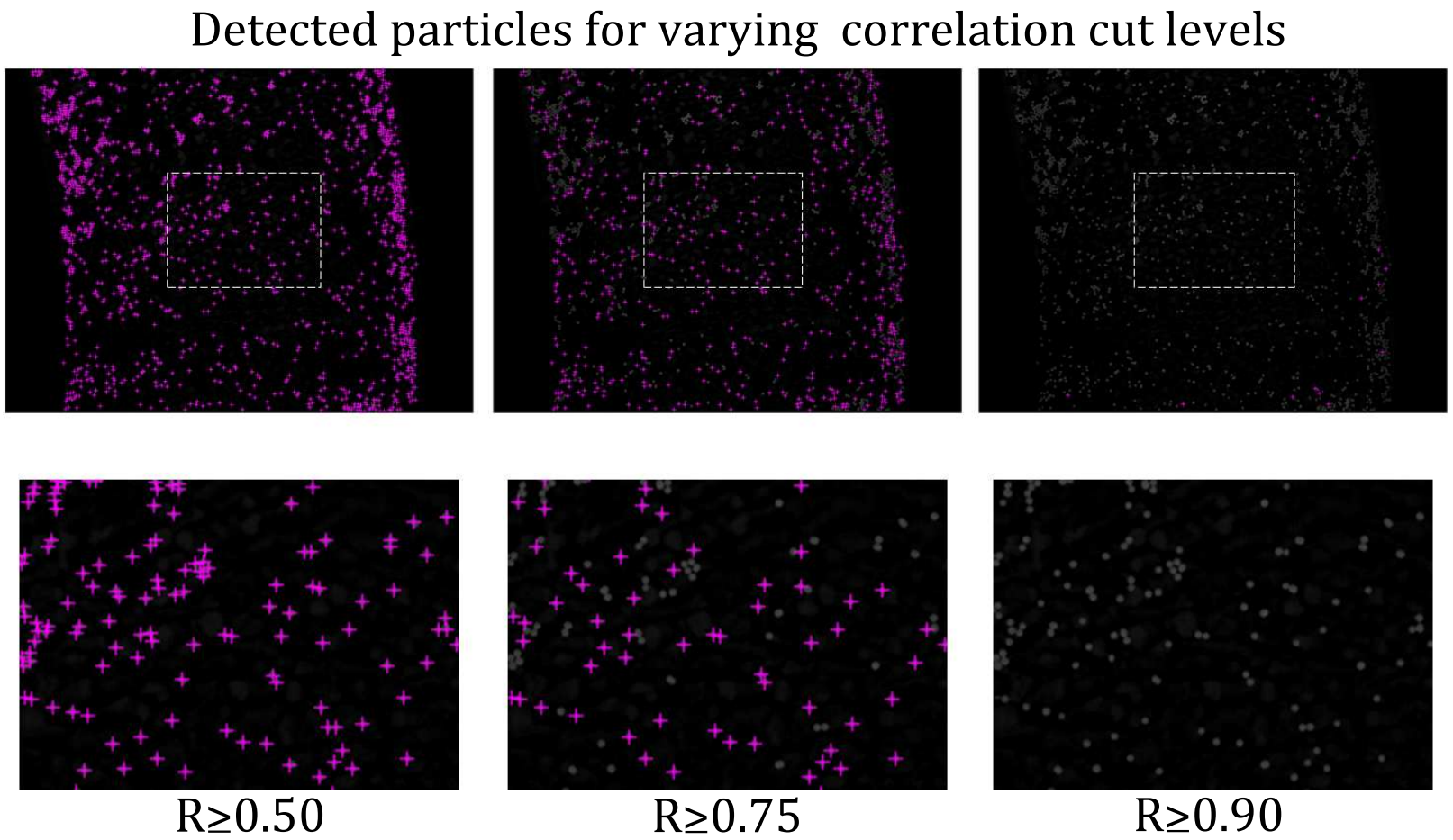

Figure 3.7: Images showing the effect of the correlation cut level in the number of particle centroids found by the algorithm. Crosshairs indicate that a centroid has been detected.

might be the same particle identified in the first frame which will be referred hereafter as the target particle. When candidates are defined, matching between one of them and the target particle in frame one is made. From the matching, a displacement vector can be determined and with the time between frames velocity can be computed.

3.4.1 Finding Candidate Particles

Two basic methods can be used to find candidate particles in the second image. The first one consists on defining a number of candidates in the area of the target particle search for them beginning from the closest to the one farthest away. The second method defines a window (an area) around the target particle and considers as candidates those particles inside that window regardless of the number. Once candidates are defined, their coordinates are passed along with the target particle coordinates to the matching routine.

3.4.2 Matching the Particles

The matching in this study is done by using the highest cross correlation coefficient obtained after comparing a reference light intensity matrix in the first frame (centered on the target particle) and a set of sub-matrices at the second frame (centered on the candidate particles). The size of the matrices is defined by an interrogation window whose size is based on the expected particle displacement between the images.

The cross correlation coefficients are calculated using Eq. (3.10).

$$R = \frac{\sum_m \sum_n (a_{mn} - A)(b_{mn} - B)}{\sqrt{\sum_m \sum_n (a_{mn} - A)^2 \sum_m \sum_n (b_{mn} - B)^2}} \tag{3.10}$$

Where:

R **-** is the cross correlation coefficient.

a *and* b **-** are matrices of size $m \times n$.

A *and* B **-** are the mean values of light intensity of all the elements in matrices a and b respectively.

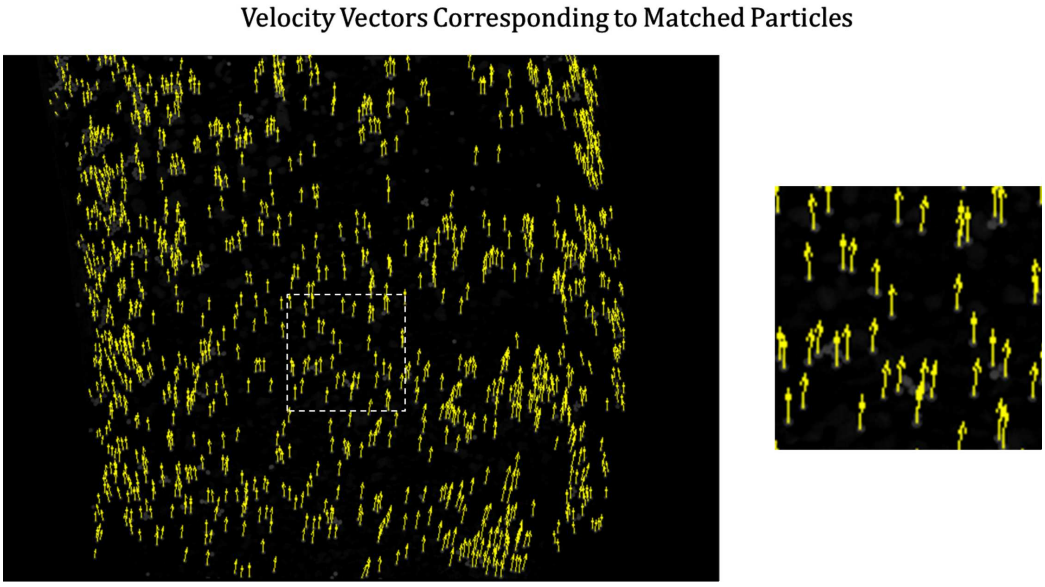

Figure 3.8: Resulting velocity vectors determined by the algorithm for a correlation coefficient of 0.75.

Two filtering stages are performed on all matched particles. The first stage uses a cross-correlation threshold similar to the one used in the particle detection routines. All matched particles with a cross-correlation coefficient higher than the threshold value will be accepted and the rest will be discarded.

The second filter used is to avoid double matches. If a candidate particle has two target particles its displacement vector is compared to that of neighboring particles. The criteria assumes that a particle's displacement should be similar in magnitude and direction to that of neighboring particles and therefore out of the two possible matches, the one that compares better with the neighbors is kept while the other is discarded. Figure 3.8 shows the resulting vectors determined by the algorithm for a case in which the correlation coefficient was set to 0.75.

3.5 Image Post-Processing Routines

Up to the previous stage in the process, particles that were detected and successfully matched contain information that is randomly located in space.

In addition, velocity data obtained through the matching of particles is in units of pixels/time. In order to obtain adequate velocity measurements in units of length/time and in a structured way, the information must be post-processed. A description of the main steps ensues.

3.5.1 Interpolating Results to a Grid

The results obtained through the particle matching routines are randomly located across the image plane due to the nature of the technique. Every pair of images in the series has an independent set of vectors associated to it and its configuration is dependent on the random locations of particles in the original images. Therefore, in order to obtain structured information out of the images, the results are interpolated to a grid with specified dimensions. The routine requires both the time interval between pictures (given by the frame rate, e.g. 50 Hz) and the length of a pixel in the image. With that information coupled with the results from previous stages it determines the velocity vector at each grid point by interpolating the result from neighboring pixels.

Determining the length of each pixel requires a calibration image which must be taken every time the camera has been moved or if the distance between the lens and the water surface has changed (e.g. if flow or water depth have changed). The calibration image uses a target which consists of a set of equally spaced dots in the vertical and horizontal directions. Figure 3.9 shows an example of the calibration image used in this study which had equally-spaced dots at 1 cm intervals.

3.5.2 Determining the Mean Velocity and Vorticity Maps

The process of computing the velocity vectors at a regularly spaced grid provides a structured velocity distribution for each pair of images in the series. In order to obtain the mean velocity and vorticity maps, all image pairs in the set need to be taken into account. However, some image pairs might

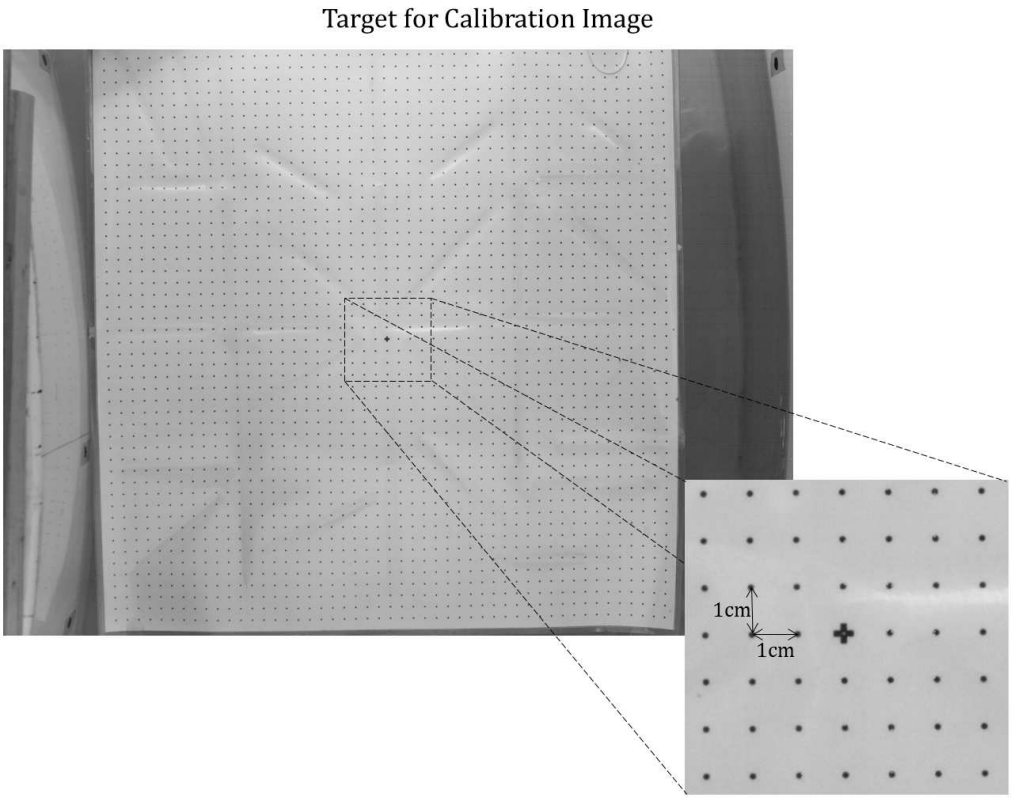

Figure 3.9: Example of calibration image with target on the water surface.

not have information at specific locations of the image plane because at that particular time there were no particles flowing through them.

This is taken into account when computing the average by making sure that the denominator in the averaging routine at each grid point adds up to only the amount of images in the series that have data at that location. Failing to do so would yield lower velocity values at those grid points where the particle density was not constant throughout the imaging time period. In order to characterize the mean flow, several sets of image series must be taken and then the mean flow velocities are computed for the ensemble. In this study, ten sets were taken at each location and averaged to obtain the mean flow. The surface vorticity matrix which can be used to detect the presence of strong shear regions and vortices was computed as the *curl* of the mean velocity matrix.

CHAPTER 4

2D DEPTH-AVERAGED MODELING

The three different width-to-depth ratio experimental measurements conducted in this study are also used to validate a 2D depth-averaged model called STREMR (Bernard (1993)). Of particular interest is to asses its secondary flow correction. Note however that the model's results are integrated over the depth while the measurements were made only at the water surface.

4.1 Model Description

The hydrodynamic model STREMR (Bernard (1993)) provides discrete solution of the incompressible Navier-Stokes equations for 2D depth-averaged flow. The depth-averaged flow in channels of arbitrary shape is computed by taking into account the mutual interactions between sidewalls, obstacles and bathymetry. The primary input required by the code includes a computational grid (mesh), optional inflow and outflow velocity distributions along user-specified boundaries and enough depth data to reconstruct the bathymetry by interpolation. Manning's n is the only empirical parameter required as part of the code's input.

STREMR includes a $k - \epsilon$ two-equation turbulence model and a three-dimensional (3D) correction to account for secondary flow in bends. The former generates an eddy viscosity from the computed primary flow and the latter accounts for the interaction between vertical non-uniformity and curvature, which is responsible of causing high velocities to migrate towards the outer bank of channel bends.

Irregular 2D flow boundaries are accounted for by STREMR by using a finite-volume discretization scheme with curvilinear grids. It also accounts

for non-uniform bathymetry by letting the user assign a different depth to each grid cell. STREMR might be used under varying bathymetry as long as the depth-induced forces vary gently enough with position. If this is true, then the 3D effects can be approximated with the depth-averaged corrections for bottom friction and secondary flow.

Free surface subcritical flows with local Froude numbers as high as 0.5-0.7 can be modeled with STREMR even though it imposes a rigid-lid approximation. Regardless of this assumption, the pressure computed by the model is equivalent to the displacement of a free surface and therefore it can be used as an approximation for it. The rigid-lid approximation becomes more accurate as the local Froude number gets lower.

4.2 Characterizing the Flume's Roughness

In order to assess the performance of the numerical model, several scenarios were tested taking into account only the turbulence capabilities first and then including the secondary flow correction. Both routines contain empirical coefficients that were calibrated by Bernard and Schneider (1992) and Bernard (1993) in order to account for near wall turbulence, flow separation zones and low depth-radius of curvature ratios among others. Assuming that the coefficients proposed by Bernard (1993) are adequate for the flow being modeled then Manning's n is the only empirical coefficient to be input in the model.

With this in mind, the first goal was to obtain an accurate value to characterize the roughness of the flume. To achieve this goal, the following set of equations were used. First, Eq. (4.1) was used to determine the hydraulic radius R_h which depends on the width B and depth H of the flow. Once computed, the shear velocity u_* can be determined with Eq. (4.2). The slope of the water surface S_e was measured for each case in the laboratory by taking the bed and water surface elevations at CS0 and CS30.

$$R_h = \frac{BH}{B + 2H} \tag{4.1}$$

$$u_* = \sqrt{gR_hS_e} \tag{4.2}$$

Using the reach averaged flow velocity U computed with Eq. (4.3) where Q is the flow inside the flume, the Chezy coefficient C_z was determined for each width-to-depth ratio condition through Eq. (4.4).

$$U = \frac{Q}{BH} \tag{4.3}$$

$$C_z = \frac{U}{u_*} \tag{4.4}$$

The Chezy coefficient allows obtainig the friction coefficient C_f and Manning's n with Eq. (4.5) and Eq. (4.6) respectively where g is the acceleration of gravity.

$$C_f = \frac{1}{C_z^2} \tag{4.5}$$

$$n = \frac{R_h^{1/6}}{C_z\sqrt{g}} \tag{4.6}$$

Using the relations above, Manning's n for all three cases was determined and the result is shown in Table 4.1 along with the intermediate values. Note however that this roughness values are reach-averaged and therefore they not only represent the roughness of the flume's surface but account for the curvature and skewness of the flume, i.e. the geometry, which provides additional resistance to the flow. This means that the highest Manning's n that could be used to model each flow is the one presented in the table but in reality a lower value could be used to decouple the surface roughness from the geometric roughness.

4.3 Numerical Grid

Before running any numerical model a discrete representation of the geometry is required. STREMR contains a routine that requires as input the coordinates of the points located at the North-South and East-West boundaries to create the numerical grid. Once the grid is created the model can be ran by specifying the input parameters in a text file following the format required by the main executable. The first grid used was generated by dividing the flume centerline in 5 cm intervals in the streamwise direction

Table 4.1: Roughness coefficients for each width-to-depth ratio condition and intermediate values needed to compute them.

Width-to-depth ratio [−]	Depth $H[m]$	Hydraulic radius $R_h[m]$	Flow $Q[L/s]$	Reach-averaged velocity $U[m/s]$	Water surface slope $S_e\ x10^{-4}[-]$	Shear velocity $u_*[m/s]$	Chezy coefficient $C_z[-]$	Friction coefficient $C_f[-]$	Manning's $n[s/m^{1/3}]$
2.4	0.25	0.136	25	0.17	0.51	0.008	20.2	0.0024	0.011
4.0	0.15	0.100	25	0.28	3.96	0.020	14.1	0.0050	0.015
12.0	0.05	0.043	8	0.27	7.32	0.018	15.2	0.0043	0.012

(see Figure 4.1(a)). In the transverse direction 16 elements were used with smaller elements close to the wall to resolve better the flow separation zones and wider elements close to the center of the flume where changes between adjacent cells are not as drastic as those occurring close to the wall.

After an initial set of runs it was learned that the mesh needed to be refined even more for the case where the width-to-depth ratio was 12.0. The mesh elements in some cases were larger than the water depth and therefore errors in the computation occurred. A refined mesh (see Figure 4.1(b)) was used for this case with twice as much elements in the streamwise direction (spaced 2.5 cm in the centerline) and in the transverse direction 24 elements were used instead of the original 16. Comparison of the two grids used is presented in Figure 4.1.

4.4 Setting Up and Running

STREMR's executable requires a namelist input file with the parameters for the run. The code reads the parameters based on their name within a given namelist in the input file. In general a run requires three namelists which should appear in order even though the specific parameters within them can be randomly located. Not all parameters need to be input since STREMR will assign default values for most of them.

The first namelist is called 'BEGIN' which is used to describe characteristics of the run such as if it should start from a previous computed result or from zero. The namelist 'PARAM' is the second one and it is used to specify the units in which the output should be printed, the number of time steps for the computation, the time step to be used as well as to define if the user wants to switch on/off the turbulence model and the secondary flow correction. Empirical constants pertaining to these routines can also be modified in this namelist.

The third namelist is called 'INPUT' and can be used repeatedly for the input of grid cell types, general (global) values, section values, line values and single-cell values of the initial flow variables. Being a rigid-lid model,

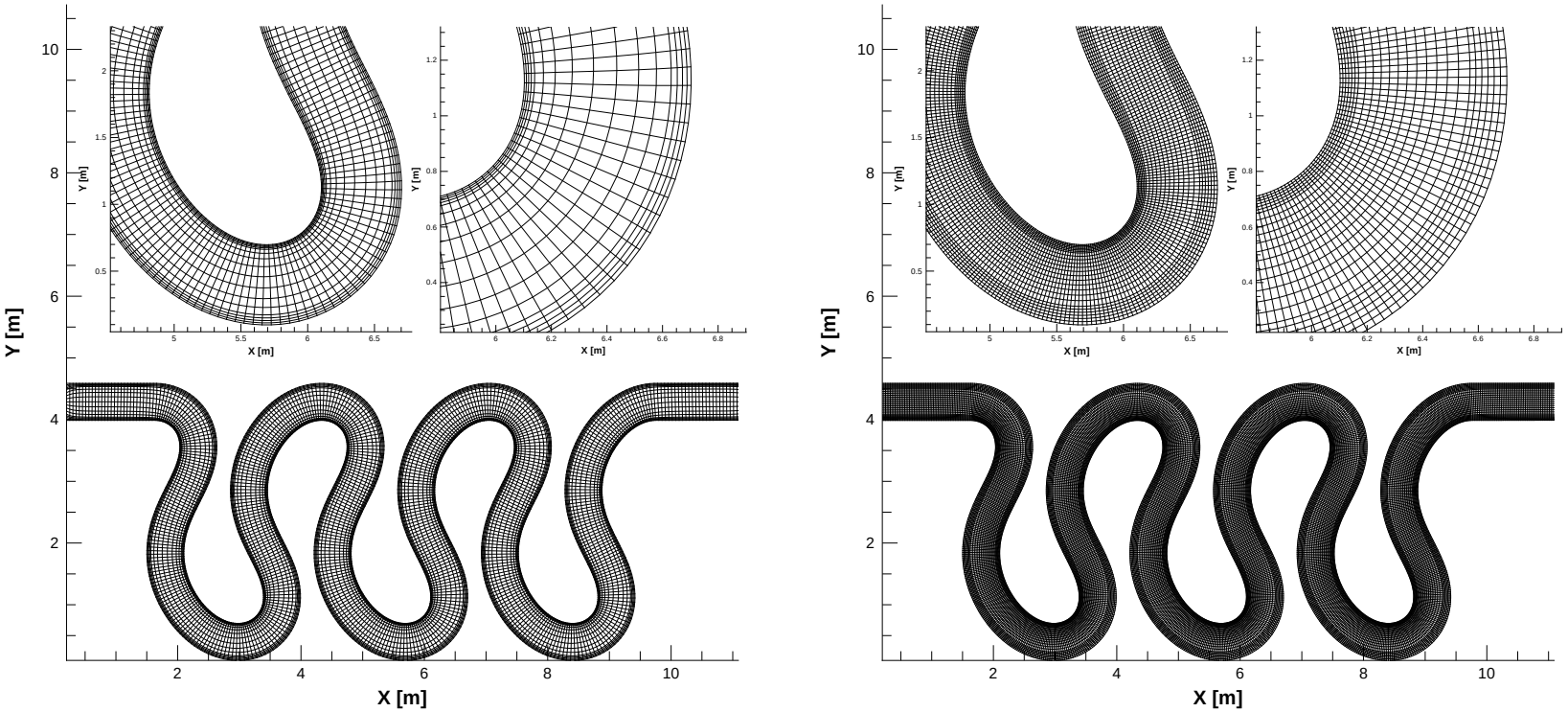

(a) (b)

Figure 4.1: Computational grid used in the model. The (a) coarse mesh was used for the first two width-to-depth ratios (2.4 and 4.0) and the (b) fine mesh was used for the higher width-to-depth ratio (12.0).

the water surface elevation is imposed through this namelist by setting the elevation at the upstream and at the downstream ends of the mesh. STREMR will interpolate the values in between. Other parameters that can be set in this namelist are Manning's n, initial velocity values and flowrate for the run.

The main parameters used for the validation of the model with the experimental measurements are presented in Table 4.2. The values shown correspond to the final cases that were run which yielded the best results.

Table 4.2: Summary of most important parameters used for the final modeling run scenarios.

Parameter	Units	Value		
Width-to-depth ratio	[-]	2.4	4.0	12.0
Flow	$[m^3/s]$	0.025	0.015	0.008
Manning's n	$[s/m^{1/3}]$	0.015	0.011	0.012
Upstream water depth	[m]	0.2526	0.1567	0.063
Downstream water depth	[m]	0.2543	0.1436	0.038
Water surface slope $x10^{-4}$	[-]	3.96	0.51	7.32
Turbulence	[-]	YES	YES	YES
Secondary Flow Correction	[-]	YES	YES	YES
Number of time steps	[-]	10,000	10,000	100,000
Time step	[s]	0.01	0.01	0.001

4.5 Secondary Flow Correction

Vertical motion in the flow can not be accounted for in 2D depth-averaged models. However, in a general sense, when the depth-averaged streamlines of a flow are curved, centripetal forces create a torque in the streamwise direction that generates helicity in the flow. The helicity pattern creates an out-of-plane (vertical) motion that can be described by a shear stress which may affect the depth-averaged flow. To account for this vertical inhomogeneity of the flow in curved channels STREMR has an empirical correction.

In a general sense and following Bernard (1993) the forces applied to an element of fluid are described by Eq. (4.7) where **T** represents the viscous

forces, $\mathbf{X}$ represents the friction forces and $\mathbf{S}$ represents the secondary force.

$$\mathbf{F} = \mathbf{T} - \mathbf{X} + \mathbf{S} \tag{4.7}$$

The secondary force in STREMR is approximated with Eq. (4.8) and note that as shown in Eq. (4.7) it adds up to the viscous forces. This means that the helical secondary flow creates shear stress in excess of that produced by viscosity.

$$\mathbf{S} \approx \frac{1}{\rho}\frac{\mathbf{u}}{|\mathbf{u}|}\left[\frac{1}{h}\mathbf{n}\cdot\nabla\left(h\tau_s\right) + \frac{1}{r}2\tau_s\right] \tag{4.8}$$

where

ρ – Fluid density.

$\mathbf{u}$ – Velocity vector (u, v).

h – Flow depth.

$\mathbf{n}$ – Unit vector normal to $\mathbf{u}$.

∇ – Gradient operator $\left(\frac{\partial}{\partial x}, \frac{\partial}{\partial y}\right)$.

τ_s – Secondary shear stress.

r – Local radius of curvature.

The normal derivative of the depth-integrated secondary shear stress is given by the scalar product $\mathbf{n}\cdot\nabla(h\tau_s)$ (see Eq. (4.9)) and the radius of curvature is related to the velocity derivatives by Eq. (4.10).

$$\mathbf{n}\cdot\nabla(h\tau_s) = \frac{1}{|\mathbf{u}|}\left[v\frac{\partial h\tau_s}{\partial x} - u\frac{\partial h\tau_s}{\partial y}\right] \tag{4.9}$$

$$r = \frac{|\mathbf{u}|^3}{uv\left[\frac{\partial v}{\partial y} - \frac{\partial u}{\partial x}\right] + u^2\frac{\partial v}{\partial x} - v^2\frac{\partial u}{\partial y}} \tag{4.10}$$

All terms in the equations above are known from the depth-averaged computations except for τ_s, the shear stress associated with the secondary flow. This term is the one that is determined empirically in STREMR and the assumptions and equations to do it are presented next.

Let $\mathbf{u}'(z)$ be a perturbation of the depth-averaged velocity vector $\mathbf{u}$. The perturbation takes place in the vertical direction z and it must satisfy the constraint in Eq. (4.11).

$$\int_{-h/2}^{h/2} \mathbf{u}' dz = 0 \tag{4.11}$$

where

$z = h/2$ – Water surface level (rigid lid).

$z = -h/2$ – Channel (flume) bottom level.

The velocity vector $\mathbf{u}$ can be modified by expressing it as a mean velocity plus a perturbation, $\mathbf{u} + \mathbf{u}'$ when deriving the depth-averaged momentum equation. By doing so a perturbation of the depth-integrated shear stress arises given by Eq. (4.12)

$$h\tau' = -\rho \int_{-h/2}^{h/2} u'v' dz \tag{4.12}$$

where

u' – x-component of $\mathbf{u}'$.

v' – y-component of $\mathbf{u}'$.

Note that the perturbation stress τ_s' is not necessarily zero even though $\int u' dz = 0$ and $\int v' dz = 0$. Bernard (1993) proposed that the simplest functions that would allow $\tau' \neq 0$ and still satisfy Eq. (4.11) are the following:

$$u' = \omega_2 z \tag{4.13}$$

$$v' = -\omega_1 z \tag{4.14}$$

where

ω_1 – x-component of depth-averaged vorticity.

ω_2 – y-component of depth-averaged vorticity.

Substituting Eq. (4.13) and Eq. (4.14) into Eq. (4.12) yields

$$\tau' = \frac{1}{12}\rho h^2 \omega_1 \omega_2 \tag{4.15}$$

The y-component of the depth-averaged vorticity ω_2 can be considered roughly proportional to the square root of the friction factor (Johannesson and Parker (1989)) as shown in Eq. (4.16) where the constant of proportionality is C_2.

$$\omega_2 \approx C_2 \frac{u\sqrt{C_f}}{h} \tag{4.16}$$

Combining the previous two equations and assuming that the result is valid regardless of the direction of the velocity (i.e., replacing $\mathbf{u}$ by $|\mathbf{u}|$) then the averaged secondary shear stress can be approximated with Eq. (4.17).

$$\tau_s = \rho h \Omega \sqrt{C_f}\, |\mathbf{u}| \tag{4.17}$$

where

$$\Omega = C_2 \frac{\omega_s}{12} \tag{4.18}$$

and ω_s is the streamwise vorticity. At this point, only Ω remains as an unknown to be determined in order to compute the secondary shear stress τ_s. Consider a vertical column of water in a flow with radius of curvature r (seen from the top), streamwise velocity given by Eq. (4.19) and outward radial velocity given by Eq. (4.20).

$$u_s(z) = |\mathbf{u}| \left[1 + C_2 \frac{z}{h}\sqrt{C_f}\right] \tag{4.19}$$

$$u_r(z) = \omega_s z \tag{4.20}$$

The vertical column of flow experiences at any elevation z a centripetal acceleration u_s^2/r, due to the curvature. At the bottom of the column a radial shear stress roughly proportional to $\rho h \omega_s C_f^{1/2} |\mathbf{u}|$ is acting for which a no-slip condition and a vertical eddy viscosity proportional to the square root of the friction factor have been assumed. Conservation of angular momentum is then described by Eq. (4.21) where C_1 is a constant of proportionality.

$$\rho \frac{\partial}{\partial t} \int_{-h/2}^{h/2} \omega_s z^2 dz = -\frac{1}{2} C_1 h^2 \sqrt{C_f} \rho \omega_s |\mathbf{u}| + \rho \int_{-h/2}^{h/2} \frac{u_s^2}{r} z dz \tag{4.21}$$

Eq. (4.19) and Eq. (4.21) can be combined and integrated obtaining the result in Eq. (4.22). Eq. (4.18) can then be substituted into Eq. (4.22) to obtain an implicit relationship for the variation of Ω in time in terms of Ω

itself (see Eq. (4.23)). The equation shows the dependence of the rate of change of vorticity in time with the streamwise velocity, the friction factor, the depth, the radius of curvature and vorticity itself.

$$\frac{\partial \omega_s}{\partial t} = 2C_2\sqrt{C_f}\frac{|\mathbf{u}|^2}{rh} - 6C_1\sqrt{C_f}\omega_s\frac{|\mathbf{u}|}{h} \tag{4.22}$$

$$\frac{\partial \Omega}{\partial t} = \frac{1}{6}C_2^2\sqrt{C_f}\frac{|\mathbf{u}|^2}{rh} - 6C_1\sqrt{C_f}\Omega\frac{|\mathbf{u}|}{h} \tag{4.23}$$

The form of Eq. (4.23) is a consequence of (a) having imposed the centripetal and frictional forces on the vertical column of water and (b) the assumption of the z-dependence of the out-of-plane and streamwise velocities. The relation is only of qualitative value unless the arbitrary constants C_1 and C_2 are inferred from experimental data. Note that the right-hand side of Eq. (4.23) contains empirically derived terms for production and dissipation of Ω. If Ω is regarded as being truly proportional to ω_s, then the governing equation should include terms for diffusion and vortex-stretching as well. This latter term, proportional to $\Omega \cdot \nabla \mathbf{u}$, will be insignificant compared to the advection term $\mathbf{u}\cdot\nabla\Omega$ as long as $|h\Omega| << |\mathbf{u}|$. With the empirical coefficients rearranged and turbulent diffusion added Eq. (4.23) yields Eq. (4.24) which is a depth-averaged relation for the time rate of change of Ω where $A_s = 5.0$ and $D_s = 0.5$ (Bernard and Schneider (1992)).

$$\frac{\partial \Omega}{\partial t} = A_s\sqrt{C_f}\frac{|\mathbf{u}|^2}{rh} - D_s\sqrt{C_f}\Omega\frac{|\mathbf{u}|}{h} + \frac{\nu}{h}\nabla\cdot(h\nabla\Omega) + \nabla\nu\cdot\nabla\Omega \tag{4.24}$$

The first term on the right-hand side is the production term. It is followed by the dissipation term and two more terms which correspond to vortex diffusion and vortex advection respectively. When the depth of the flow is comparable in magnitude to the radius of curvature of the flow's streamlines then the production term may yield values that are larger than what is physically acceptable. To prevent this from happening Bernard (1993) adopted a self-limiting function such that the computed values for the production term would be reasonable for low or high width-to-depth ratios. The expression can be used for a wider variety of flows since it is not limited to shallow flows and its purpose is to dampen the secondary flow production term when flows are deep. The final relation used inside STREMR is given by Eq. (4.25). Note that when $h << r$ the relation would yield approximately the same value as

the previous one, however when the depth and the radius of curvature are equal, the production term would be reduced by an order of magnitude.

$$\frac{\partial \Omega}{\partial t} = A_s \sqrt{C_f} \frac{|\mathbf{u}|^2}{rh\left(1 + 9\frac{h^2}{r^2}\right)} - D_s \sqrt{C_f} \Omega \frac{|\mathbf{u}|}{h} + \frac{\nu}{h} \nabla \cdot (h \nabla \Omega) + \nabla \nu \cdot \nabla \Omega \quad (4.25)$$

Eq. (4.17) and Eq. (4.25) are the equations used for the secondary flow correction in STREMR. More details on their implementation can be found in Bernard (1993).

CHAPTER 5

RESULTS AND DISCUSSION

Experimental and numerical results are presented and analyzed in this chapter. The mean surface velocities measured for the three different width-to-depth ratios are shown first followed by the results regarding the surface vorticity maps for the same conditions. Finally, the results from the 2D depth-averaged model (STREMR) validation are discussed.

5.1 Mean Surface Velocities

The results presented in this section correspond to the mean surface velocity measurements taken with the Particle Tracking Velocimetry (PTV) technique on the middle bend of the Kinoshita flume. Reference will be made to particular locations along the flume for which cross sections have been previously defined (e.g. Ancalle (2007), Abad and Garcia (2009a)). Figure 5.1 shows the cross section locations along the flume and the highlighted area corresponding to the middle bend of the flume (CS10 to CS20) is where the measurements were taken. The surface velocity contour maps for all cases are presented first followed by the corresponding vector fields. The last subsection addresses the normalized surface velocity values obtained. Along the discussion, reference to zones of high or low curvature along the flume will be made. Figure 5.2 presents the values of the radius of curvature and curvature for the flume along the measured region (CS10-CS20).

5.1.1 Surface Velocity Contours

Figure 5.3 shows the mean surface velocity magnitude contours for the three width-to-depth ratio cases measured. The three are presented using the same scale for comparison purposes. Note that all three cases present the core of

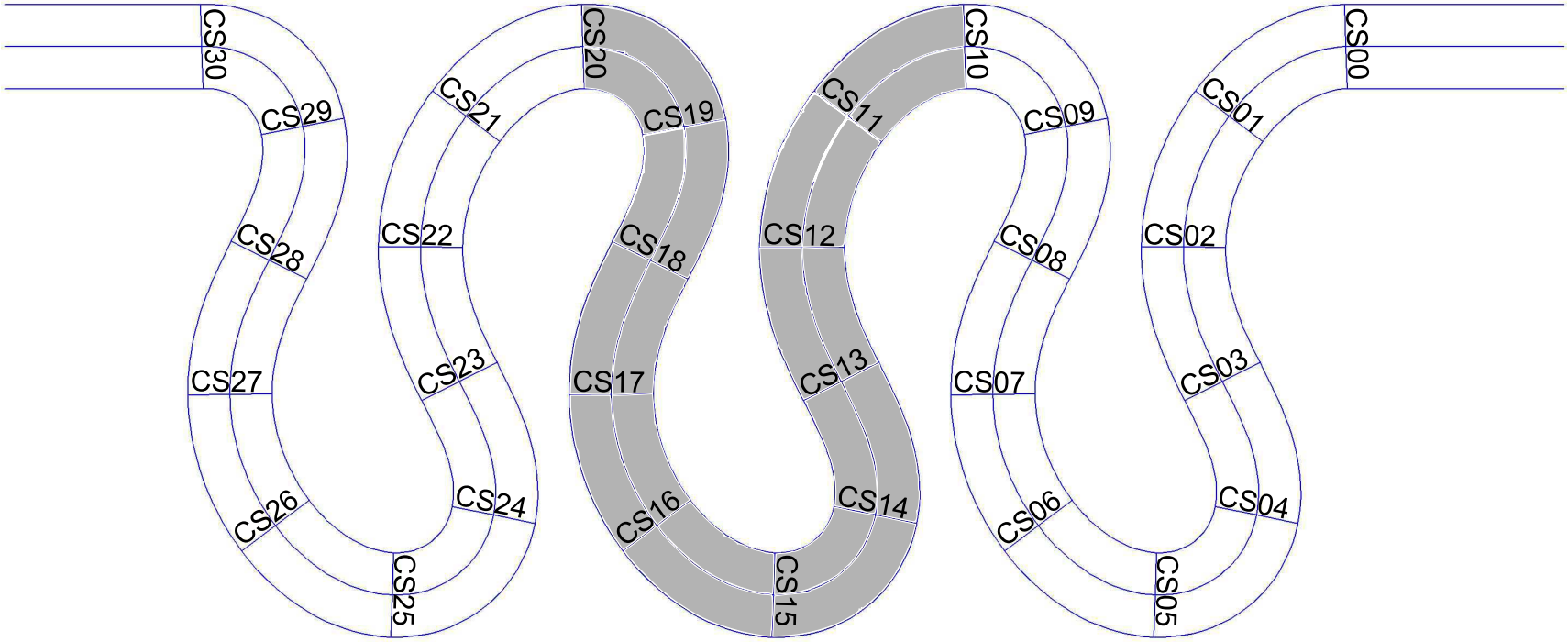

Figure 5.1: Kinoshita flume sketch showing the location of the cross sections. Surface velocity measurements were taken between CS10 and CS20 which is the middle bend. Flow in all cases entered the flume upstream of CS00 and exited downstream of CS30.

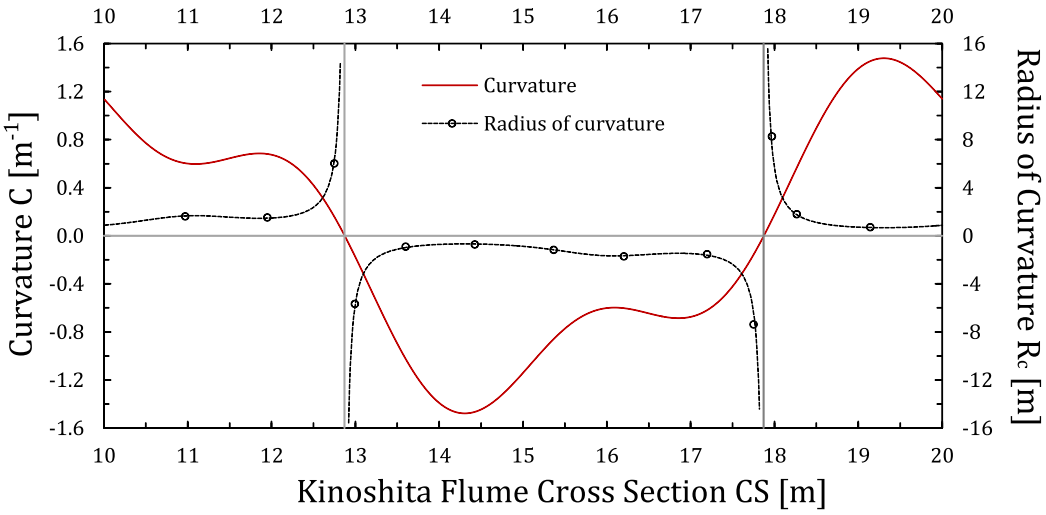

Figure 5.2: Curvature and radius of curvature along the middle bend of the Kinoshita flume (between CS10 and CS20).

high velocities at the inner bank. This was expected due to the fact that experiments were carried out on non-movable flat bed conditions. For this type of configuration (curved channel and flat bed) super elevation of the flow occurs at the outer part of the bend and since the inner region has a smaller depth, the flow velocity increases to satisfy continuity. The highest velocities observed in all three cases occur at the points of highest curvature, i.e. approximately between CS14-CS15 and CS19-CS20. In general, the velocity patterns observed can be described as follows. A region of high curvature (between CS09 and CS10) precedes the measurement section and therefore, as the flow enters the region, it has a core of high velocities on the inner bank which is already vanishing as shown by the contour maps (see in particular the yellow region immediately after CS10 in Figure 5.3(b)). It is easier to observe for the case in which the width-to-depth ratio has a value of 4.0 but it is still recognizable in the other two cases.

As the flow progresses downstream and after it passes CS11, it enters a region of lower curvature values where the turnover in velocity occurs. Higher velocities that were present in the left bank begin to move towards the right bank but before doing so a region of uniform velocities should be observed where the curvature of the flume has a value of zero. In the case of the Kinoshita flume this occurs just before CS13 and the measured values show

approximately uniform velocity patterns between CS12 and CS13.

The curvature in the flume increases fast and reaches a maximum value at the apex, slightly after CS14. At this point, the highest velocities along the inner bank are observed in all three cases. The core of high velocities extends until about CS15 where it begins to vanish again and a zone of flow separation is seen (the three cases have regions of slowly moving flow in the inner bank after CS15). The core of high velocities begins to move towards the outer bank due to the secondary flow cell circulation which is responsible for pushing it outward. Approximately at CS16 it is about one third of the channel width away from the right (inner) bank.

In this second part of the middle bend, the point of inflection (zero curvature) occurs slightly before CS18 and the apex is located after CS19. Therefore, the velocity turnover described above for the first half of the bend occurs between CS17 and CS18 whereas the core of high velocities is observed between CS19 and CS20.

5.1.2 Surface Velocity Vector Fields

Velocity vectors for all width-to-depth ratio conditions are presented here. Some of the patterns described above are easier to observe with the vector fields (see Figure 5.4). Again, same scale was used for all cases to allow comparison on similar grounds. Note that on all three cases, between CS10 and CS11 the vanishing core of high velocities is present close to the inner bank. Of particular interest is that in the third case which can be considered a shallow flow condition (see Figure 5.4(c)), the higher velocities are farther away from the bank than they are in the other two cases. This suggests that the secondary flow intensity is higher for shallow flows, thus pushing harder the core of high velocities towards the outer bank.

For the smallest width-to-depth ratio case (see Figure 5.4(a), after CS10 the core of high velocities is still close to the bank and by CS11 it has retreated but at a lower rate than what was observed for the other two cases. Note that for the shallow flow case, the higher velocities have almost moved

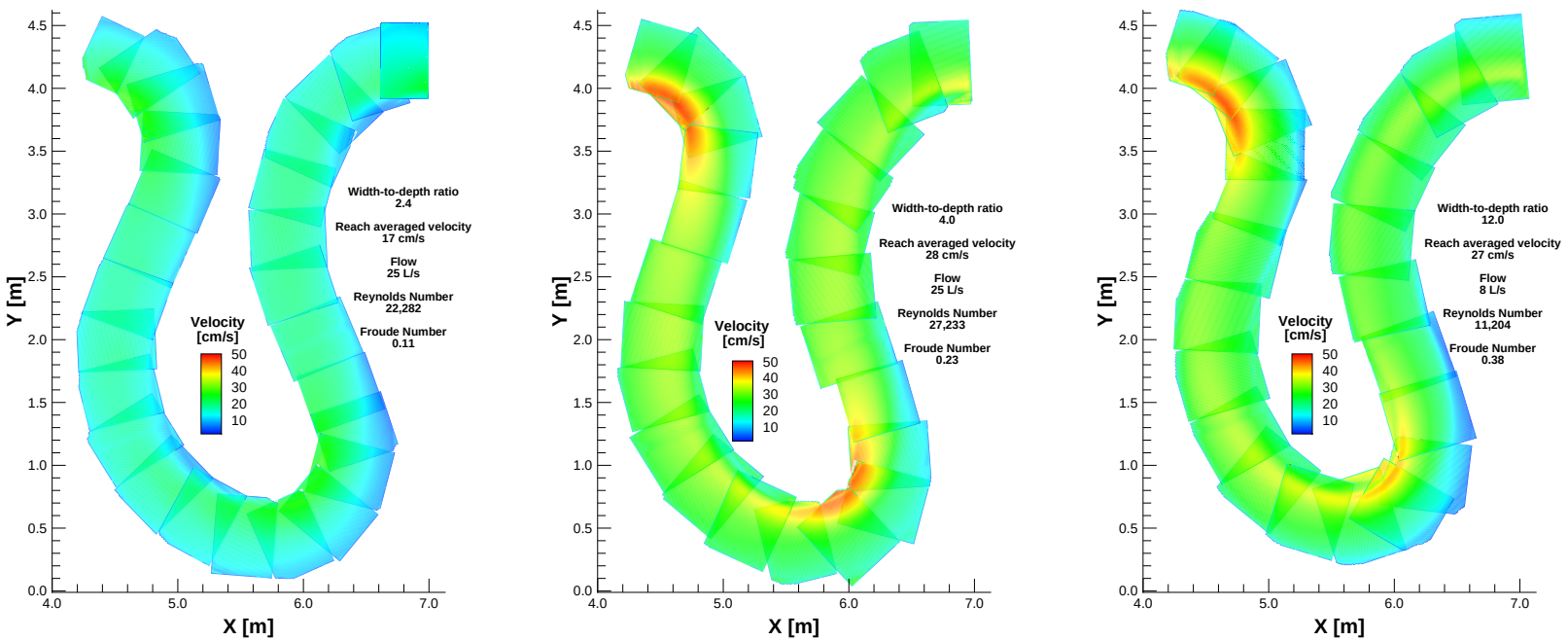

(a) (b) (c)

Figure 5.3: Mean surface velocity maps for the three width-to-depth ratios.

completely towards the outer bank shortly after CS11 but this is not the case for the other flow conditions which are not shallow.

It was stated before that a region of uniform velocity should be expected close to CS13 where the curvature of the flume is zero and therefore no velocity differences across the cross section would be expected. Nevertheless, the vector fields suggest that the velocity turnover, at least at the surface, occurs at different locations depending on the width-to-depth ratio. The deepest flow condition seems to be the one for which the turnover happens first (closer to CS12), however in all cases the turnover occurs between CS12 and CS13.

After the turnover, a core of high velocities begins to appear in the neighborhood of CS14. The differences between the inner and outer bank velocities for the first case (Figure 5.4(a)) is gradual and less dramatic than for the other two cases which show inner bank velocities significantly higher than those observed at the outer bank. Comparing the second and third cases, it is important to highlight that they have similar reach-averaged velocities but both the Reynolds and Froude numbers are different.

Focusing in the region between CS14 and CS15 it is seen that the second case (Figure 5.4(b)) has higher velocities than the third case (Figure 5.4(c)). Considering the ratio of inertial to viscous forces (i.e. the Reynolds Number), the former case has a ratio that is 2.5 times larger than the latter suggesting that viscous forces have an effect on the distribution of velocities in the bend. This might be the case for the Kinoshita flume but is not something that should be extrapolated to real meandering rivers since the Reynolds numbers there are certainly in the fully turbulent region.

Comparing the same two cases (width-to-depth ratios of 4.0 and 12.0), the shallow flow condition has a velocity gradient that covers the whole width of the flume between CS14 and CS15 whereas the other one shows approximately constant velocities on the outer third of the width. This suggests that the intensity of the secondary flow cell in the shallow case will be higher because the velocities vary across the whole width of the flume.

Regarding flow separation after the apex, it is seen again that in the case of the shallow flow it happens faster. Secondary flow is responsible for pushing the core of high velocities away from the inner bank. In the first case, even after CS15, the core of high velocities is still close to the inner bank ('hugging' the bend) but in the other two cases at CS15 a small region close to the inner bank presents lower velocities. On the other hand, for the shallow flow case, by CS16, the core of high velocities is already in the middle of the channel. For the width-to-depth ratio of 4.0, at CS16 the core of high velocities is about one third of the width away from the inner bank, i.e. moving slower towards the outer bank.

All cases present the region of uniform velocity (where the turnover takes place) between CS17 and CS18. The turnover occurs earlier (closer to CS17) for the case in which the width-to-depth ratio is 2.4 suggesting that the intensity of the secondary flow in the other two cases delays its occurrence. Approaching the end of the measurement region, another core of high velocities is observed between CS19 and CS20 for all cases. Patterns observed are similar to those described for the other apex between CS14 and CS15.

5.1.3 Normalized Surface Velocity Contours

The normalized surface velocity results are presented in Figure 5.5. The results look very similar which suggest that the geometry of the channel plays a role in the distribution of flow despite the differences in width-to-depth ratio, reach-averaged velocity, Reynolds and Froude numbers. If sediment were present the results might not be as similar. First of all the core of high velocities would be observed at the outer bank but regardless of that, in the presence of a movable bed the flow configuration would also be affected since not all flows would equilibrate to the same morphological characteristics of the bed which would induce differences in the velocity patterns.

The flow patterns across the bend described in previous sections are still observed here. Note that in general, the core of high velocities in all three cases presents velocities greater than 1.5 times the mean and approaching values of 2.0 in particular in the apex located between CS19 and CS20. Lower

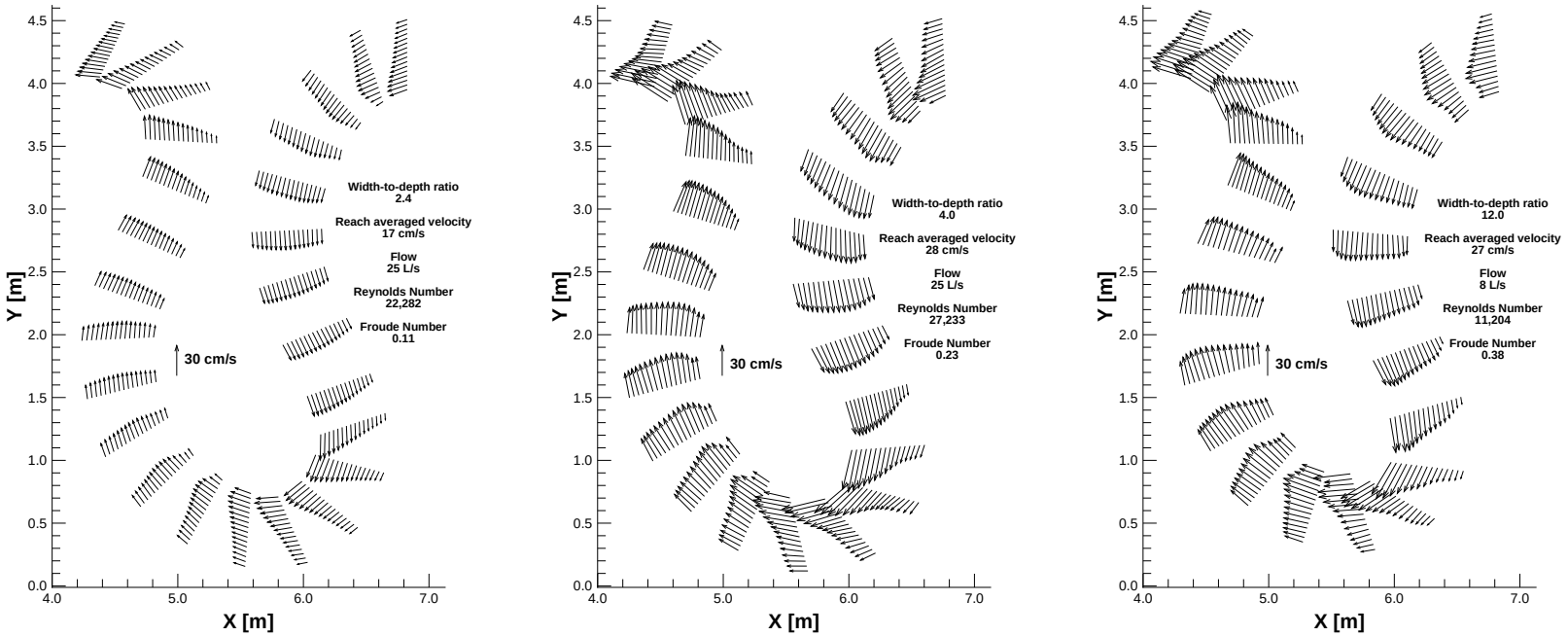

(a) (b) (c)

Figure 5.4: Mean surface velocity vectors for the three width-to-depth ratios.

velocities are observed at the apex located between CS14 and CS15. This is due to the fact that the flow is slightly deeper at this region than it is at the downstream location. In terms of the transversal velocity distribution, the flow sections where the curvature is high present the largest velocity gradients and these are more notorious for the shallow flow case (see Figure 5.5(c)) indicating that the differences between inner and outer bank velocities are higher for shallow flows than they are for deeper flows. Some regions in the width-to-depth ratio case of 12.0 have velocities as low as 10% the reach-averaged velocity whereas in the case where it is 2.4, the lower velocities are on the neighborhood of half its value.

Another aspect to be highlighted is the movement of the core of high velocities form the inner to the outer bank. In general, the core of high velocities (see yellow colors) in the shallow case covers a longer region. It starts developing almost at CS13 and is still noticeable at CS17. On the other hand, even though the core of high velocities for the first case also appears at CS13, it vanishes by CS16. In this latter case where the flow is deeper and the secondary flow intensity is also smaller, the core of high velocities remains closer to the inner bank. Comparing the last two cases (Figure 5.5(b) and Figure 5.5(c)) which have approximately the same reach-averaged velocity it is seen that the core of high velocities in the last case moves faster towards the outer bank. This was also mentioned above but it is easier to observe in the normalized velocity maps.

5.2 Mean Surface Vorticity

The mean surface vorticity field of all cases is presented in Figure 5.6. These fields were obtained by computing the *curl* of the mean velocity values ($\omega = \nabla \times \mathbf{u}$) presented in Figure 5.3. Vorticity fields serve two purposes. The first one is that vortex cores contain concentrated regions of vorticity and their presence could be identified by the vorticity field. The second one is that regions of strong shear in the absence of structure are also identified by vorticity fields. In this case, the vorticity fields will then allow observing

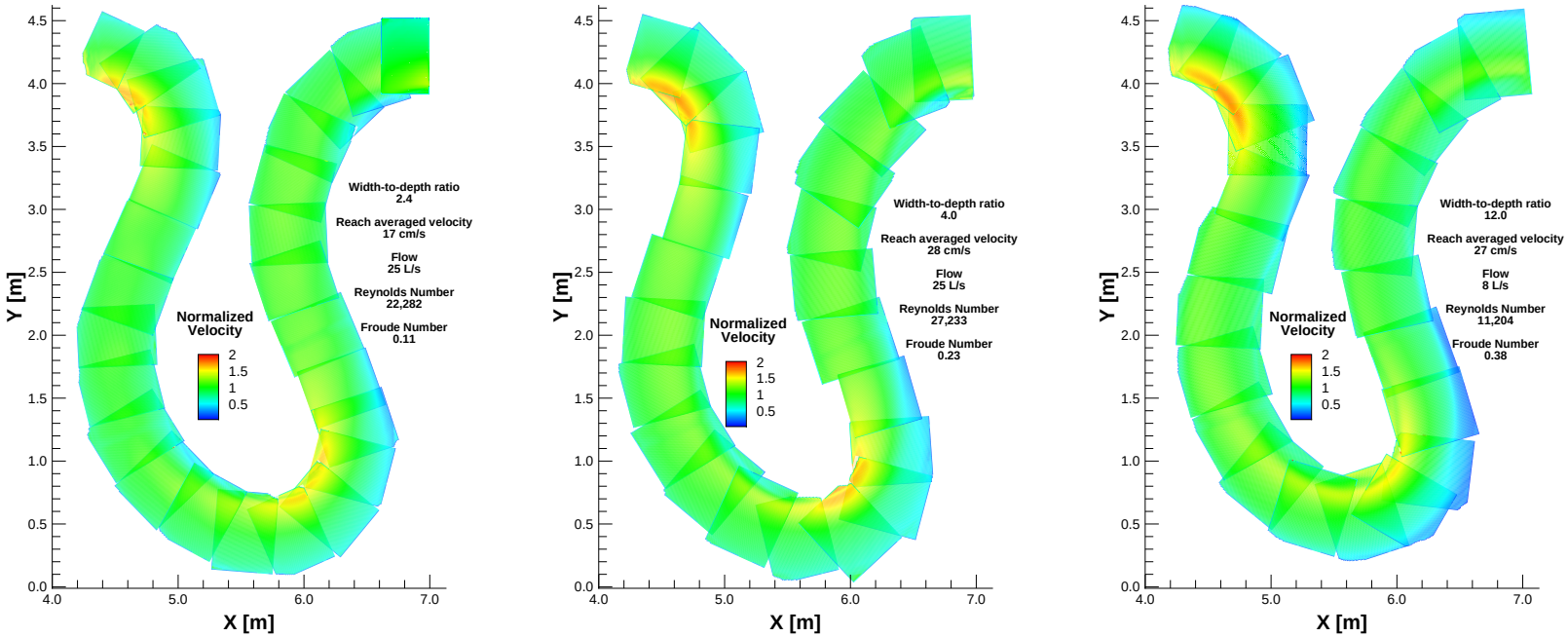

(a) (b) (c)

Figure 5.5: Normalized mean surface velocity maps for the three width-to-depth ratios.

the regions where vortices are present but will also reveal the areas where shear regions (e.g. flow separation regions) are present. Due to the nature of the measurements, the vorticity fields are noisy at the edges of the images but in general, patterns and trends can be distinguished. Positive vorticity values are associated with counter-clockwise rotations and are represented by the warm colors (yellow and red) whereas negative vorticity values, shown in cool colors (light blue and blue) correspond to clockwise rotations.

The first case, corresponding to the lowest width-to-depth ratio (Figure 5.6(a)) presents smaller vorticity regions than the other two cases. They are located close to the apexes and extend a little bit downstream suggesting the occurrence of flow separation. The other two cases have more intense vorticity fields and in general suggest the presence of vortices or shear regions across the full bend. Note that in the shallow flow case (Figure 5.6(c)), the positive vorticity values after CS15 extend far away from the wall and cover half the width of the flume by CS16. A similar pattern is observed with the negative values at CS11.

Another interesting aspect observed is the presence of both negative and positive vorticity values for the shallow flow case covering the regions that preceed or follow the highest curvature points. Between approximately CS12 and CS14 vorticity fields are present near the wall suggesting shear and as the flow approaches the apex, the negative vorticity region moves away from the wall and reaches the middle of the channel suggesting also a slower moving area of flow. This was observed before with the velocity vector fields and it also becomes apparent here.

Finally, the highest vorticity values covering wider regions are present in the shallow flow condition where different phenomena interact to enhance the shear regions and vortex formation (e.g. flow separation, secondary flow intensity). That said, note that the second case presents also high vorticity values and in this case its similarity with the shallow flow condition might be due to its higher Reynolds number. This higher Reynolds number indicates more turbulence, thus higher deviations from the mean flow are expected and they appear in the vorticity fields.

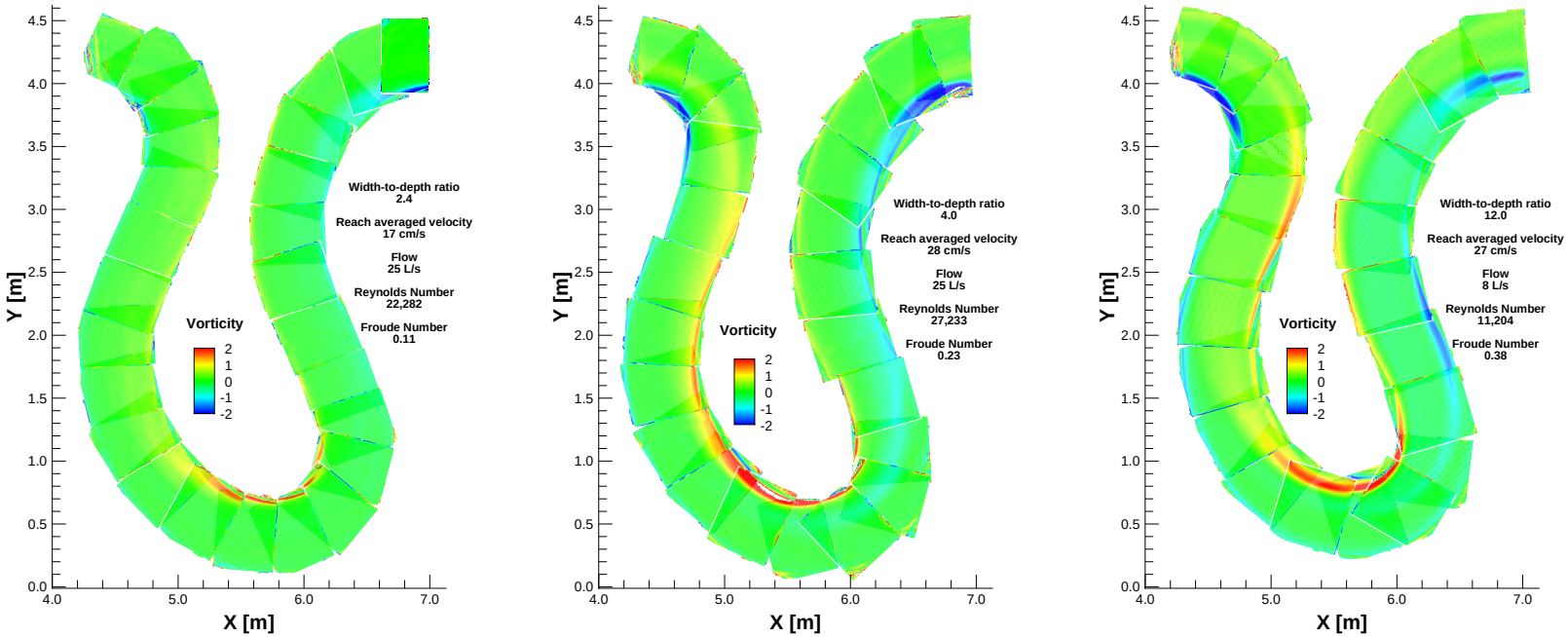

(a) (b) (c)

Figure 5.6: Mean surface vorticity maps for the three width-to-depth ratios.

5.3 Model Validation

The results obtained with STREMR are compared in this section with those measured in the flume. Note however that the goal here is not to match them perfectly since the model computes a depth-averaged flow whereas the measurements correspond to the surface of the flow only. Before presenting the comparison some details regarding the secondary flow correction in STREMR and the Kinoshita flume are discussed.

5.3.1 Secondary Flow Correction in STREMR and the Kinoshita Flume

A description of STREMR was given in Ch. 4 and of particular interest to the Kinoshita flume and the three width-to-depth ratio cases analyzed here is the secondary flow correction routine described in Sec. 4.5. It was shown (see Eq. (4.25)) that the correction for secondary flow contains a production term which must be dampened when the depth of the flow scales with the radius of curvature. For the first two cases considered here where the width-to-depth ratios are 2.4 and 4.0 this is needed to avoid over predicting the velocities observed.

The production term in Eq. (4.25) can be expressed as a scaling factor (given by the inverse value of the denominator) times the other parameters ($A_s\sqrt{C_f}|\mathbf{u}|^2$). The standard scaling factor is given by $[rh]^{-1}$ and the self-limiting factor is given by $[rh(1+9h^2/r^2]^{-1}$ where r is the radius of curvature and h is the flow depth. Figure 5.7 shows the behavior of the standard and the self-limiting scaling factors on the production term of the secondary flow as a function of the radius of curvature for the three width-to-depth ratios analyzed here.

$H25$ indicates the case in which the depth was $25cm$ and the width-to-depth ratio was the smallest. Note that the self-limiting scaling factor deviates rapidly from the standard one as the radius of curvature decreases and its value is less than half of the standard one for the smallest radius of curvature in the Kinoshita flume. On the other hand, the case indicated by $H05$ corresponding to the shallow flow condition (width-to-depth ratio of 12.0)

does not present any significant differences between the standard and the self-limiting factors in the range pertaining the Kinoshita flume. Since secondary flow intensities in shallow flows are larger than those in deep flows there is a need to prevent from over predicting them in deep flows. Therefore the self-limiting function must be used.

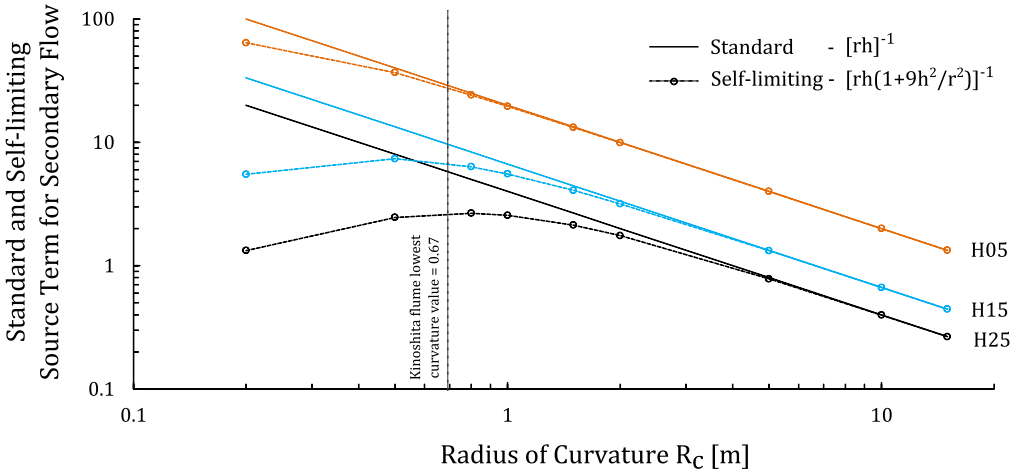

Figure 5.7: Standard and self-limiting scaling factor for the production term of secondary flow shear stress as a function of the radius of curvature for the three width-to-depth ratios. The minimum radius of curvature value in the Kinoshita flume is indicated. Note that r represents the radius of curvature and h the flow depth.

Figure 5.8 presents the ratio of the self-limiting factor versus the standard factor at specific cross sections in the Kinoshita flume. Recall from Figure 5.2 that the regions of zero curvature (infinite radius of curvature) are located approximately at CS13 and CS18 whereas the higher curvature values (low radius of curvature) are located between CS14-CS15 and CS19-CS20.

In the regions where the radius of curvature is high, the secondary flow intensities are small and therefore both standard and self-limiting functions present similar values regardless of the width-to-depth ratio. However, at other cross sections such as CS14, CS15, CS19, CS20 they differ more from each other. Note however that in the shallow flow case the self-limiting factor is still within 5% of the standard factor but in the deeper flow case -$H25$- (width-to-depth ratio of 2.4) the self-limiting factor decreases to about half the standard case value. Again this is due to the fact that secondary flow

intensities in deep flows are smaller than in shallow flows and the differences are accounted for through the self-limiting factor in STREMR.

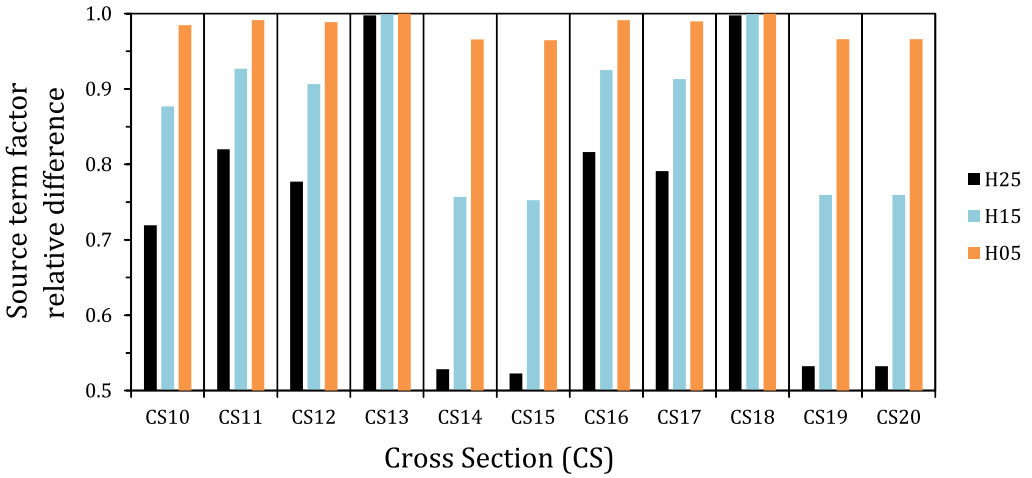

Figure 5.8: Relative difference of the source term for production of secondary flow. The ratio between the self-limiting factor to the standard one is presented.

5.3.2 Modeled and Measured Results Comparison

Comparison between the modeled (depth-averaged) and measured (surface) velocity contours for the three width-to-depth ratios is presented in Figure 5.9, Figure 5.10 and Figure 5.11. Even though the full Kinoshita flume was modeled with STREMR, comparison is made only in the middle bend. All three cases present the same patterns than the measured values. The velocities from the depth-averaged model are lower than those measured at the surface and even though Manning's n could have been modified to match them perfectly that was not the goal. Manning's n values used were calculated in Sec. 4.2 and presented in Table 4.1.

STREMR is able to capture the flow patterns in the flume and the secondary flow correction accounts for the differences between deep and shallow flows. In the first case presented in Figure 5.9 the core of high velocities stays attached to the inner bank after the apex (close to CS15) before mov-

ing towards the outer bank. Close comparison of the three cases shows that in the shallow flow case (see Figure 5.11) the secondary flow plays a major role in pushing the core of high velocities towards the outer bank. In the case of the smallest width-to-depth ratio the higher velocities stay in the middle region of the flume's width before the turnover and reach the other bank until after CS18. On the other hand, the highest width-to-depth ratio has a core of high velocities that moves faster to the outer bank and reaches it approximately at CS16. It then stays there until the next apex. Similar behavior was observed in the surface for the three cases and is also shown in the figures.

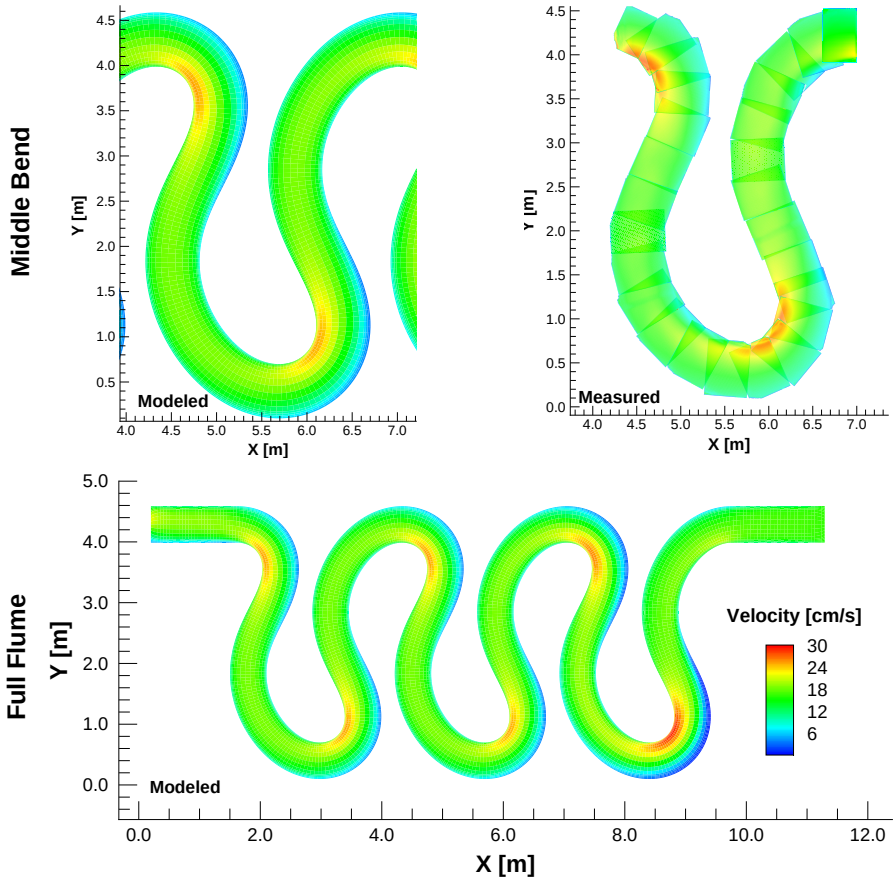

Figure 5.9: Velocity contours for the full flume (bottom) and the middle bend (top). The modeled contours correspond to depth-averaged values while the measured ones (top-right) correspond to the surface values. The width-to-depth ratio used in this case was 2.4.

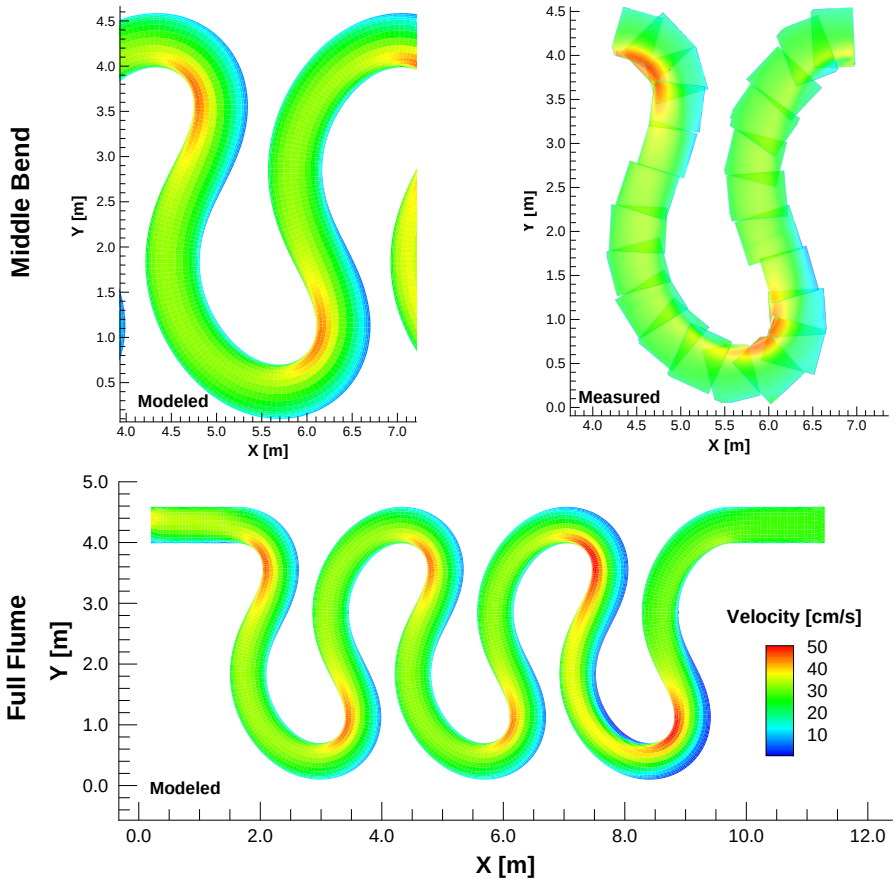

Figure 5.10: Velocity contours for the full flume (bottom) and the middle bend (top). The modeled contours correspond to depth-averaged values while the measured ones (top-right) correspond to the surface values. The width-to-depth ratio used in this case was 4.0.

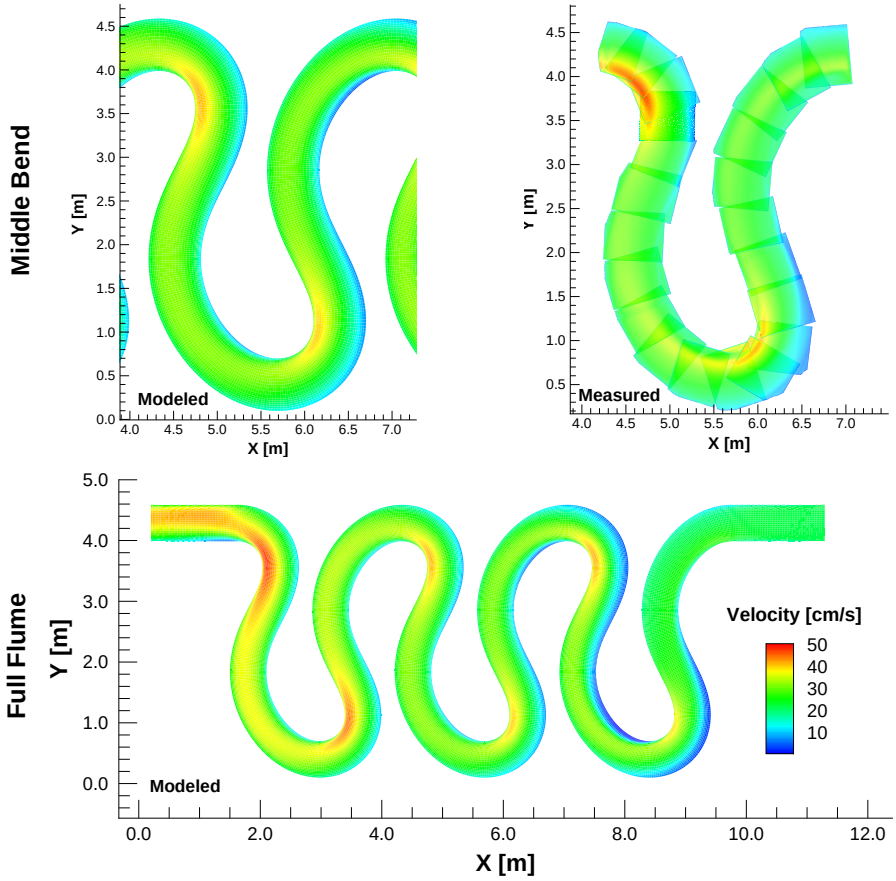

Figure 5.11: Velocity contours for the full flume (bottom) and the middle bend (top). The modeled contours correspond to depth-averaged values while the measured ones (top-right) correspond to the surface values. The width-to-depth ratio used in this case was 12.0.

The three cases were normalized using the reach-averaged velocity to improve the comparison among them. The results are presented in Figure 5.12, Figure 5.13 and Figure 5.14 starting with the smallest width-to-depth ratio. Again, the figures indicate that the depth-averaged velocities predicted by the model are slightly slower than those measured at the water surface. In general, the flow patterns and velocity gradients between inner and outer banks present the same magnitudes and the locations of flow separation and high velocity cores are the same.

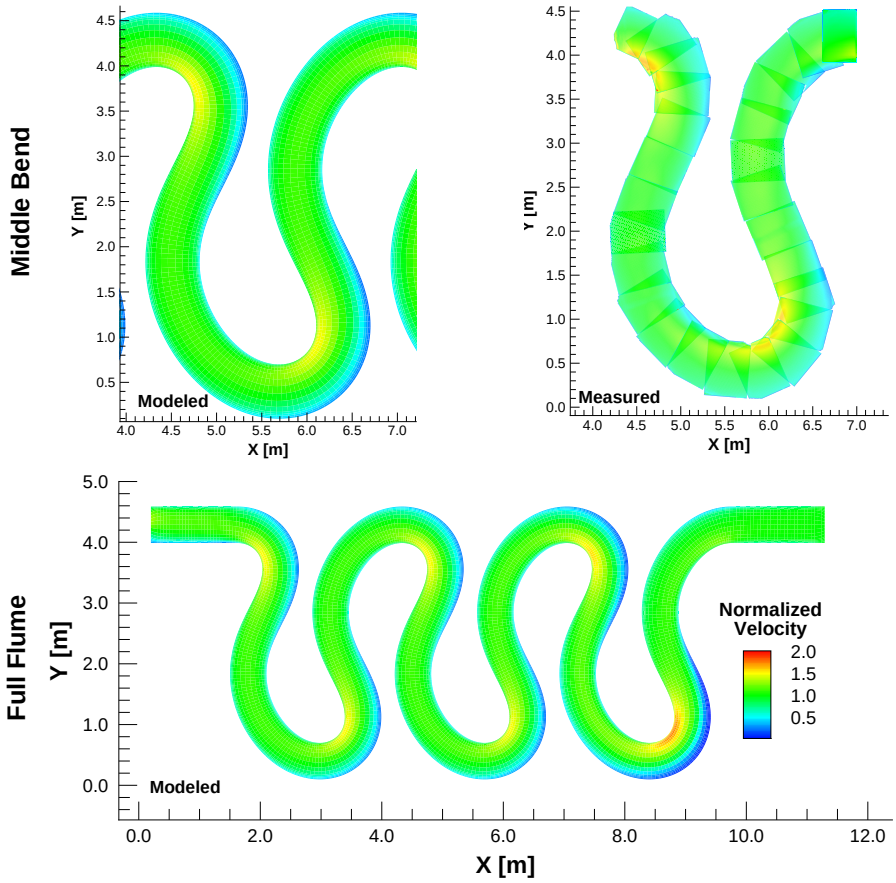

Figure 5.12: Normalized velocity contours for the full flume (bottom) and the middle bend (top). The modeled contours correspond to depth-averaged values while the measured ones (top-right) correspond to the surface values. The width-to-depth ratio used in this case was 2.4.

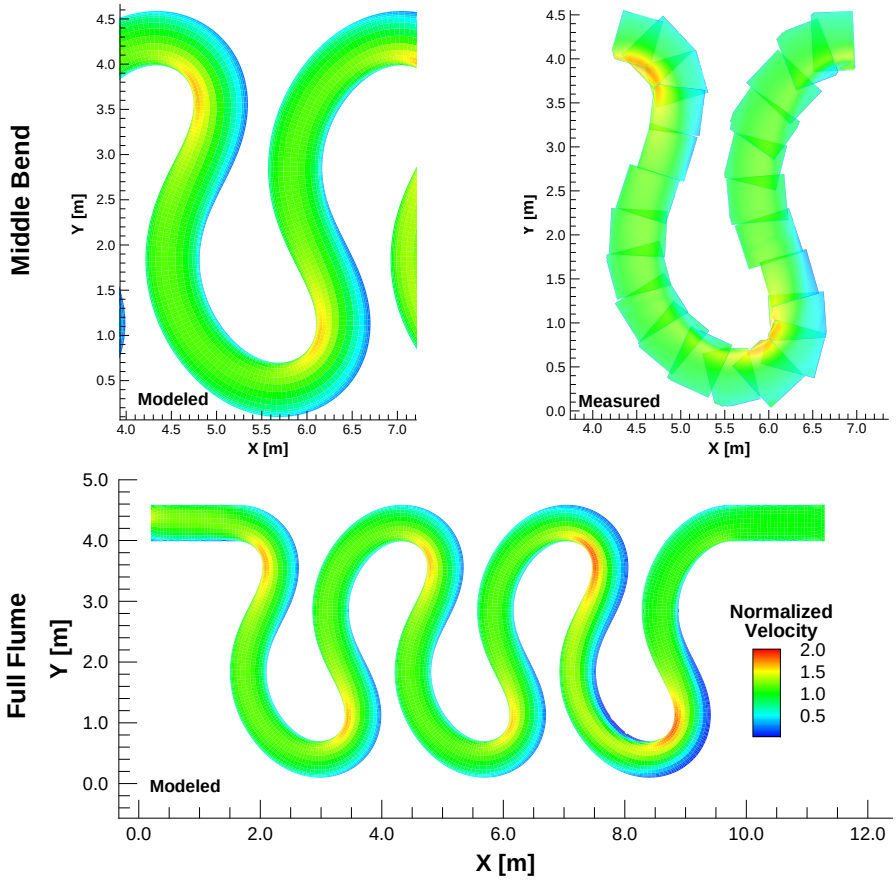

Figure 5.13: Normalized velocity contours for the full flume (bottom) and the middle bend (top). The modeled contours correspond to depth-averaged values while the measured ones (top-right) correspond to the surface values. The width-to-depth ratio used in this case was 4.0.

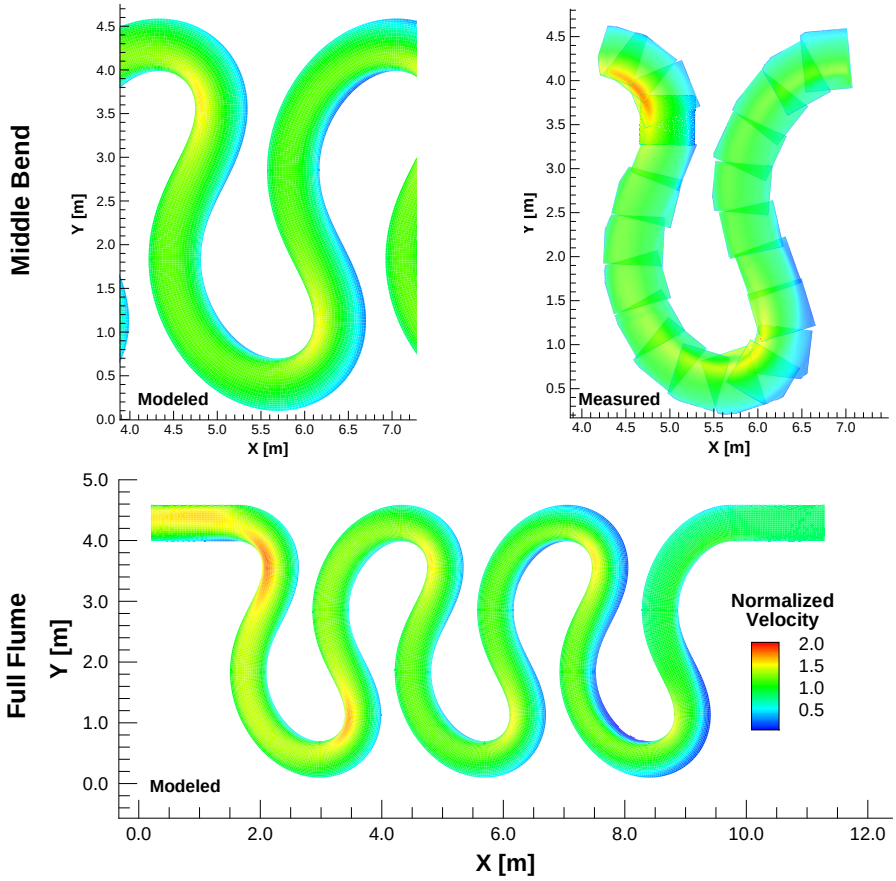

Figure 5.14: Normalized velocity contours for the full flume (bottom) and the middle bend (top). The modeled contours correspond to depth-averaged values while the measured ones (top-right) correspond to the surface values. The width-to-depth ratio used in this case was 12.0.

CHAPTER 6

CONCLUSIONS AND RECOMMENDATIONS

The following conclusions can be drawn from the work presented in this document

1. Particle Tracking Velocimetry (PTV) was successfully used to obtain mean surface flow characteristics for three different width-to-depth ratios in the Kinoshita flume.

2. PTV is a useful technique to measure flows in cases where there is need for a non-intrusive technique or where the characteristics of the flow impede the use of other options such as Acoustic Doppler Velocimeters.

3. Image pre-processing (image inversion, background removal, masking) is a crucial aspect required to improve the quality of the results and to minimize the computational times required to process the multiple image series.

4. Sensitivity of parameters in the particle detection routines such as the light intensity threshold level and the correlation coefficient must be determined before analyzing the full series of images in order to prevent the algorithm from detecting things that are not particles.

5. Particle matching routines also require a preliminary analysis of the parameters involved to prevent the algorithm from matching erroneous particles and to avoid cases in which only a small number of particles is successfully matched by the algorithm.

6. Surface flow patterns in a non-movable flat bed in the Kinoshita flume present cores of high velocities at the inner banks of bends mainly due to the effect of super elevation of the flow.

7. Higher velocity gradients between inner and outer banks occur in shallow flows whereas in deep flows the velocity variations between both banks is smaller and less dramatic.

8. The size of the core of high velocity along the apexes is larger in the case of larger width-to-depth ratios (shallower flows).

9. The core of high velocities in deeper flows remains closer to the inner bank longer than in the case of a shallow flow.

10. Secondary flow is more intense in shallow flows than it is in flows with very low width-to-depth ratio.

11. Secondary flow intensity is responsible for pushing the core of high velocities away from the inner bank.

12. Velocity turnover occurs in areas of the flume where the curvature values approach zero but does not happen at the same location for different width-to-depth ratios.

13. Secondary flow intensity delays the velocity turnover and therefore appeared earlier in the deepest flow condition.

14. Vorticity fields serve two purposes; namely, they show the regions where vortices are present and they also show the regions where strong shear is present.

15. Vorticity fields were more intense in the zones where flow separation is expected in the Kinoshita flume.

16. The vorticity field magnitudes and area of the deeper flow (width-to-dept ratio of 2.4) was significantly smaller than for the other two cases.

17. Normalized surface velocity values for all three width-to-depth ratios were similar due to the geometry of the flume and the absence of a movable bed which would affect each case differently.

18. Velocities observed in the inner bank at the region of high velocities in the three cases were in excess of 1.5 times the reach-averaged flow velocity. The outer bank presented velocities that were below 0.5 times the reach-averaged velocity in the same cross section.

19. The 2D depth-averaged rigid-lid model STREMR was successfully used to model the Kinoshita flume for the three width-to-depth ratios considered in this study.

20. The roughness of the Kinoshita flume was characterized for all three cases obtaining friction factors, Chezy coefficients and Manning's n values that were appropriate to model them with STREMR.

21. The secondary flow correction in STREMR uses an empirical shear stress formulation that takes into account the friction factor of the flow, the velocity magnitude, the radius of curvature of the flow's streamlines and the flow depth.

22. The secondary flow correction in STREMR contains a self-limiting factor that becomes important when the depth of the flow scales with the radius of curvature.

23. The self-limiting factor successfully dampens the production term in the secondary flow correction to prevent computing values that are not feasible when the width-to-depth ratio of the flow is small.

24. STREMR was validated against the experimental measurements by obtaining similar velocity distributions and magnitudes in all three cases.

25. STREMR's depth-averaged results in general were smaller than the surface velocities measured.

26. STREMR was capable of reproducing the flow separation regions as well as the fact that the secondary flow intensity in shallow flows pushes the core of high velocities faster towards the outer bank.

27. STREMR could be used to model other conditions in the Kinoshita flume.

After analyzing the differences between three width-to-depth ratio conditions in the Kinoshita flume, the following recommendations for future research are provided:

1. Determine turbulence statistics (data-permitting) to evaluate the differences in surface turbulence between the three cases.

2. Perform the same experiments using a rough non-movable bed to observe its effect on the flow distribution at the surface.

3. Perform the same experiments with a fixed but realistic bathymetry (not flat) to assess the effects of topographic steering on the secondary flow and its effect on the surface flow patterns.

4. Compare the measurements of the case in which the width-to-depth ratio used was 4.0 with those of Ancalle (2007) and Abad and Garcia (2009a) to determine if the surface measurements could be used to describe or at least infer the patterns observed across the flow depth.

5. Perform the same experiments using a movable bed (after it has reached equilibrium) to determine if the behavior is similar or not between the different width-to-depth ratios.

6. Assess the k-ϵ model in STREMR and do some sensitivity analysis on its coefficients to evaluate its performance in flows of high curvature such as those in the Kinoshita flume.

7. Model other width-to-depth ratio conditions with STREMR to gain further insight on the behavior of the secondary flow correction and how it pushes the core of high velocities from the inner bank towards the outer bank.

REFERENCES

Abad, J. D., Buscaglia, G. C., and Garcia, M. H. (2008). 2D stream hydrodynamic , sediment transport and bed morphology model for engineering applications. *Hydrological Processes*, 1459(August 2007):1443–1459.

Abad, J. D. and García, M. H. (2004). Conceptual and Mathematical Model for Evolution of Meandering Rivers in Naturalization Processes. In *World Water Congress*, pages 1–10.

Abad, J. D. and Garcia, M. H. (2009a). Experiments in a high-amplitude Kinoshita meandering channel: 1. Implications of bend orientation on mean and turbulent flow structure. *Water Resources Research*, 45(2):1–19.

Abad, J. D. and Garcia, M. H. (2009b). Experiments in a high-amplitude Kinoshita meandering channel: 2. Implications of bend orientation on bed morphodynamics. *Water Resources Research*, 45(2):1–14.

Allen, J. R. L. (1982). Free meandering channels and lateral deposits. *Sedimentary structures Their character and physical basis*, 2:53–100.

Ancalle, J. (2007). Experimental study on the hydraulics of high-amplitude kinoshita-generated medering channels. Master's thesis, University of Illinois at Urbana-Champaign.

Baek, S. and Lee, S. J. (1996). A new two-frame particle tracking algorithm using match probability. *Experimental Fluids*, 22:23–32.

Bernard, R. S. (1993). STREMR : Numerical Model for Depth- Averaged Incompressible Flow. Technical report, US Army Corps of Engineers Waterways Experimenl Station.

Bernard, R. S. and Schneider, M. L. (1992). Depth-Averaged Numerical Modeling for Curved Channels. Technical report, US Army Corps of Engineers Waterways Experiment Station.

Blue, F. L., J. H. J. K. and Lancefield, R. L. (1934). Flow around a river bend investigated. *Civil Engineering*, 4:1–1.

Boss, P. (1934). Anwendung der potentialtheorie auf die bewegnung des wassers in gekrmmten kanal'oder fluszstrecken. *Der Bauingenieur*, 15:1–1.

Brevis, W., N. Y. J. G. H. (2011). Integrating cross-correlation and relaxation algorithms for particle tracking velocimetry. *Experimental Fluids*, 50:135–147.

Brice, J. C. (1973). Meandering pattern of the white river in indiana an analysis. Fluvial Geomorphology.

Bridge, J. S. and Jarvis, J. (1976). Flow and sedimentary processes in the meandering river south esk, gelen clova, scotland. *Earth Surface Processes*, 1:303–336.

da Silva, A. M., El-Tahawy, T., and Tape, W. D. (2007). Variation of Flow Pattern with Sinuosity in Sine-Generated Meandering Streams. *Hydraulic Engineering*, 132(10):1003–1014.

Darby, S. E. (2002). Numerical simulation of bank erosion and channel migration in meandering rivers. *Water Resources Research*, 38:1163.

Eakin, H. M. (1935). Diversity of current-direction and load-distribution on stream-bends. Transactions, American Geophysical Union.

Eke, E. and Parker, G. (2010). Meander migration modeling accounting for the effect of riparian vegetation. EOS Transactions of AGU.

Fedorov, N. N. (1954). Experimental investigations of meander pr. *Trudy GGI*, 44:15–18.

Friedkin, J. F. (1945). A laboratory study of the meandering of alluvial rivers. Technical report, Waterways Experiment Station, U.S. Army corps of Engineers.

Garcia, M. H., Bittner, L., and Niño, Y. (1994). Mathemathical modeling of meandering streams in illinois: A tool for stream management and engineering. Hydraulic engineering Series No. 43, University of Illinois at Urbana-Champaign.

Hassan, Y., Blanchat, T., and Ch, S. (1992). Piv flow visualization using particle tracking techniques. *Measurement Science and Technology*, 3:633–642.

Howard, A. D. (1996). Floodplain processes. Wiley.

Ikeda, S., Parker, G., and Sawai, K. (1981). Bend theory of river meanders . Part 1 . Linear development. *Fluid Mechanics*, 112:363–377.

Ishikawa, M., Murai, Y., Wada, A., Iguchi, M., Okamoto, K., and Yamamoto, F. (2000). A novel algorithm for particle tracking velocimetry using the velocity gradient tensor. *Experimental Fluids*, 29:519–531.

Johannesson, H. and Parker, G. (1989). Velocity Redistribution in Meandering Rivers. *Hydraulic Engineering*, 115(8):1019–1039.

Kim, H. and Lee, S. (2002). Performance improvement of two-frame particle tracking velocimetry using a hybrid adaptive scheme. *Measurement Science and Technology*, 13:573–582.

Lancaster, S. T. and Bras, R. L. (2002). A simple model of river meandering and its comparison to natural channels. *Hydrological Processes*, 16(1):1–26.

Langbein, W. B. and Leopold, L. B. (1966). River Meanders - Theory of Minimum Variance.

Leopold, L. B. and Wolman, M. G. (1960). RIVER MEANDERS.

Lloyd, P. M., Stansby, P., and Ball, D. J. (1995). Unsteady surface-velocity field measurement using particle tracking velocimetry. *Hydraulic Research*, 33:519–533.

Mikheev, A. and Zubstov, V. (2008). Enhanced particle tracking velocimetry (eptv) with a combined two-component pair-matching algorithm. *Measurement Science and Technology*, 19:401–405.

Mockmore, C. (1944). Flow around bends in stable channels. Transactions, ASCE.

Motta, D., Abad, J. D., Langendoen, E. J., and Garcia, M. H. (2011). A simplified 2d model for meander migration with physically'based bank evolution. Geomorphology, In Press.

Nanson, R. a. (2009). Flow fields in tightly curving meander bends of low width-depth ratio. *Earth Surface Processes and Landforms*, 135(November 2009):n/a–n/a.

Nippert, H. (1930). Neuere versuche ber den strmungsvorgang in gebrmmten kanalen. *Der Bauingenieur*, 2:1–67.

Odgaard, A. J. (1986). Meander flow model. i: Development. *Hydraulic Engineering*, 112:1117–1136.

Odgaard, A. J. (1989). River-meander model. i: Development. *Hydraulic Engineering*, 115:1433–1450.

Ohmi, K. and Li, H. (2000). Particle tracking velocimetry with new algorithms. *Measurement Science and Technology*, 11:603–616.

Parker, G., D. P. A. J. (1983). Meander bends of high amplitude. *Hydraulic Engineering*, 109:1323–1337.

Parker, G. and Andrews, E. D. (1985). Sorting of Bed Load Sediment by Flow in Meander Bends. *Water Resources Research*, 21(9):1361–1373.

Parker, G., Sawai, K., and Ikeda, S. (1982). Bend theory of river meanders . Part 2 . Nonlinear deformation of finite-amplitude bends. *Fluid Mechanics*, 115:303–314.

Parker, G., Shimizu, Y., Wilkerson, G. V., Eke, E. C., Abad, J. D., Lauer, J. W., Paola, C., Dietrich, W. E., and Voller, V. R. (2011). A new framework for modeling the migration of meandering rivers. *Earth Surface Processes and Landforms*, 36(1):70–86.

Raju, S. P. (1937). Resistance to flow in curved open channels. In *Abridged Translations of Hydraulic Papers*.

Rozovskii, I. L. (1961). Flow of water in bends of open channels. Academy of Sciences of Ukranian SSR.

Ruhnau, P., Guetter, C., Putze, T., and Schnoerr, C. (2005). A variational approach for particle tracking velocimetry. *Measurement Science and Technology*, 16:1449–1458.

Schumm, S. A. and Kahn, H. R. (1971). Experimental study of channel patterns. *Nature*, 233:407–409.

Seminara, G. and Zolezzi, G. (2001). Downstream and upstream influence in river meandering. Part 1. General Theory and Application to Overdeepening. *Journal of Fluid Mechanics*, 438:183–211.

Shukry, A. (1950). Flow around bends in an open flume. Transactions, ASCE.

Thomson, J. (1876). On the Windings of Rivers in Alluvial Plains. In *Proceedings of the Royal Society of London (1854-1905)*.

Wattendorf, F. L. (1935). A study of the eff3ect of curvature on fully developed turbulent flow. In *Proceedings, Royal Society of London*, volume 148.

Whiting, P. J. and Dietrich, W. E. (1993a). Experimental constraints on bar migration trough bends: Implications foe meander wavelength selection. *Water Resources Research*, 29:4.

Whiting, P. J. and Dietrich, W. E. (1993b). Experimental studies of bed topography and flow patterns in large'amplitude meanders 1: Observations. *Water Resources Research*, 29:11.

Yarnell, D. L. and Woodward, S. M. (1936). Flow of water around 180 bends. Technical Bulletin No. 526 USDA.

Yen, B. (1965). Characteristics of subcritical flow in a meandering channel. Technical report, Institute of Hydraulic Research, University of Iowa.

Yen, C. H. and Howe, J. W. (1942). Effects of channel shape on losses in a canal bend. *Civil Engineering*, 1:1–6.

Zeller, J. (1967). Meandering channels in switzerland. In *Symposium on River Morphology*.